iScience

Article

CETSA-MS unveils novel targets engaged by rigosertib to promote anti-tumor activity and inflammatory responses

Graphical abstract

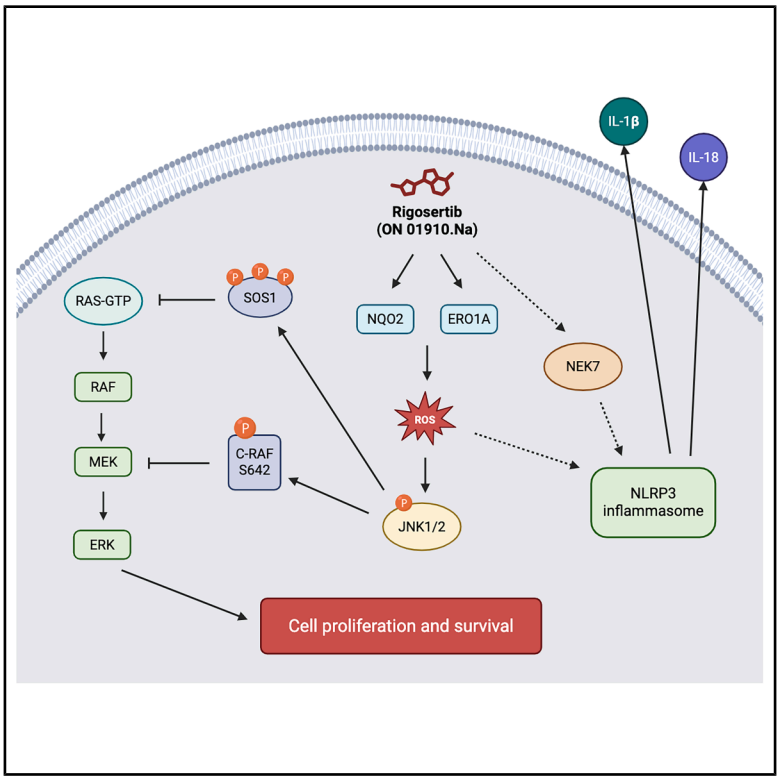

Authors

Petros Kechagioglou, Hajime Yurugi, Camille Dupont, ..., Stephen Cosenza, Steven M. Fruchtman, Krishnaraj Rajalingam

Correspondence

krishna@uni-mainz.de

In brief

Pharmacology; Biological sciences; Cancer

Highlights

- Rigosertib does not exhibit a high-affinity interaction with C-RAF RAS-binding domain
- Rigosertib exerts its inhibitory effect through ROS-induced activation of JNK signaling
- CETSA-MS identifies ERO1A and NQO2 as targets that contribute to ROS-dependent JNK activation
- Rigosertib induces NLRP3-dependent inflammatory responses in human lung cancer organoids

Kechagioglou et al., 2025, iScience *28*, 112748
June 20, 2025
https://doi.org/10.1016/j.isci.2025.112748

CellPress

iScience

CellPress
OPEN ACCESS

Article

CETSA-MS unveils novel targets engaged by rigosertib to promote anti-tumor activity and inflammatory responses

Petros Kechagioglou,[1] Hajime Yurugi,[1] Camille Dupont,[1] Alexey Chernobrovkin,[2] Rossana Romero,[1] Gregory Harms,[1] Marie Oster,[1] Sandra Ciesek,[3] Rebecca Tweedell,[4] Thirumala-Devi Kanneganti,[4] Stefanie Zimmer,[5] Stephen Cosenza,[6] Steven M. Fruchtman,[6] and Krishnaraj Rajalingam[1,7,*]

[1]Cell Biology Unit, University Medical Center Mainz, Mainz, Germany
[2]Pelago Bioscience AB, 171 65 Solna, Sweden
[3]Institute for Medical Virology, Goethe University, University Hospital Frankfurt, Frankfurt am Main, Germany
[4]Department of Immunology, St. Jude Children's Research Hospital, Memphis, TN 38105, USA
[5]Institute for Pathology, University Medical Center Mainz, Mainz, Germany
[6]Traws Pharma, Inc., Newtown, PA 18940, USA
[7]Lead contact
*Correspondence: krishna@uni-mainz.de
https://doi.org/10.1016/j.isci.2025.112748

SUMMARY

Rigosertib (RGS) is a small-molecule inhibitor known to interfere with multiple disease signaling pathways. Despite its promise as an anti-cancer drug, the exact mechanisms of its action and rational for its observed clinical efficacy remain subjects of ongoing research. Our study aimed to elucidate the mechanism of action of rigosertib and to identify its novel targets. We observed that rigosertib exerts its inhibitory effect on RAS-MAPK signaling through reactive oxygen species (ROS)-induced activation of c-Jun NH2-terminal kinase (JNK) signaling confirming previous studies. Using mass spectrometry-based cellular thermal shift assay (CETSA MS), we identified two potential novel targets, ERO1A and NQO2, which contribute to ROS-dependent JNK activation. Moreover, rigosertib induced caspase-1 activation and gasdermin cleavage leading to Nod-like receptor pyrin domain-containing 3 (NLRP3)-dependent inflammatory responses in human lung cancer organoids. Our results suggest that rigosertib may effectively inhibit RAS-MAPK signaling and reprogram the tumor immune environment, presenting the potential for a potent therapeutic strategy in cancer treatment.

INTRODUCTION

The ability of styryl benzyl sulfones to induce G2/M cell-cycle arrest and apoptosis in tumor cells has raised significant interest in their potential as cancer therapeutics.[1] Rigosertib (RGS, ON01910.Na), a styryl benzyl sulfone, was originally described as a non-ATP-competitive inhibitor of the Ser/Thr-protein kinase polo-like kinase 1 (PLK1).[2] Further analysis showed that rigosertib induced mitotic arrest, followed by tumor cell-specific induction of apoptosis. Additionally, rigosertib demonstrated a low toxicity profile and was a potent inhibitor of tumor growth in several nude mouse xenograft models.[2,3] These findings established rigosertib as a promising anticancer agent. Currently, rigosertib is undergoing a phase 2 program for advanced squamous cell carcinoma complicating recessive dystrophic epidermolysis bullosa (RDEB-associated SCC) (ClinicalTrials.gov: NCT03786237, NCT04177498). It is also being evaluated in a phase 2 trial in combination with pembrolizumab in patients with metastatic melanoma (ClinicalTrials.gov: NCT05764395) and a phase 1/2a study to examine the combination of rigosertib and nivolumab in metastatic Kirsten rat sarcoma positive (KRAS+) lung adenocarcinoma patients who have progressed on standard first line treatment (ClinicalTrials.gov: NCT04263090).

Although rigosertib was initially thought to be a PLK1 inhibitor,[4–6] this mode of action has been challenged by subsequent research showing that rigosertib does not directly inhibit PLK1 kinase activity.[7] Studies on mantle cell lymphoma (MCL) have demonstrated that 8 h of rigosertib treatment rather inhibits the PI3K/Akt/mTOR signaling pathway and triggers apoptosis via the mitochondrial pathway.[8] The ability of rigosertib to inhibit PI3K signaling was later confirmed by two studies in chronic lymphocytic leukemia (CLL) cells, and head and neck squamous cell carcinoma (HNSCC) both *in vitro* and in orthotopic xenograft models.[9,10] Similarly, Prasad et al. reported the inhibitory efficacy of rigosertib on the PI3K/Akt/mTOR pathway in preclinical HNSCC models, as well as the potential of combinatorial treatment with standard therapeutics for HNSCC.[11]

In a later study, Athuluri-Divakar et al. reported that rigosertib acts as a RAS mimetic by binding to the RAS-binding domain (RBD) of RAF protein[12] suggesting that rigosertib interferes

with the binding of active RAS to its effector proteins, thereby blocking downstream RAS signaling and tumor cell proliferation. However, a subsequent study from Ritt et al. demonstrated that the inhibition of RAS/RAF/MEK signaling by rigosertib is rather mediated by a stress-induced phospho-regulatory circuit involving activation of c-Jun NH2-terminal kinase (JNK) pathway.[13] The ability of rigosertib derivatives to bind directly to the RBD was also demonstrated by Liu et al. who showed that a rigosertib-platinum complex retained its ability to bind to RAF, displace RAS, and inhibit the RAS/REF/MEK pathway.[14] In support, Prasad et al. have previously showed that rigosertib treatment did not result in changes of p38 MAPK, RAF, and ERK1 phosphorylation status in MCL cell line but induced JNK activation.[8] The rigosertib-dependent c-JUN phosphorylation through oxidative stress induction was further confirmed in HNSCC cells, in addition to PI3K/Akt/mTOR signaling cascade inhibition.[11]

An alternative mechanism of action has been proposed by Jost et al., where rigosertib acts as a microtubule destabilizing agent by binding to tubulin at the colchicine-binding site.[15] This finding is consistent with previous results reporting that rigosertib induces cellular effects similar to those of low-dose microtubule depolymerizing agents.[7]

Rigosertib was further evaluated for its impact on tumor immune responses. In a preclinical study, a melanoma model treated with rigosertib showed enhanced response to immune checkpoint blockade therapy and promoted an inflammatory $CD8^+$ T cell response.[16] Zhou et al. demonstrated in colorectal cancer cells *in vivo* and *in vitro* that rigosertib's immunomodulatory effect results from the downregulation of PD-L1 expression and a strengthened anti-tumor immunity in the CT26 murine colorectal syngeneic tumors.[17] Accumulating data from non-cancer-related studies, reporting the rigosertib-dependent suppression of proinflammatory responses in experimental models of colitis and lipopolysaccharide-induced sepsis, respectively.[18,19]

To date, rigosertib has been demonstrated to be a well-tolerated and promising anticancer agent in clinical settings, but its precise mechanism of action remains unclear. In order to elucidate the mechanism(s) of action of rigosertib, we set out to decipher whether rigosertib's antitumor properties stem from its binding to the RBD domains of RAS target proteins, its microtubules destabilizing properties, or the inhibition of yet unidentified target(s). In addition, we investigated activation of cell death markers by rigosertib and its modulating effects on the tumor immune microenvironment.

RESULTS

Rigosertib inhibits RAS-MAPK signaling without exhibiting a high-affinity interaction with C-RAF RAS-binding domain

We first tested the hypothesis that rigosertib acts as a RAS mimetic[12] by evaluating its direct binding of clinical-grade rigosertib obtained from Onconova Therapeutics, Inc. (currently under the name of Traws Pharma, Inc.) to the RBD of C-RAF (C-RAF RBD) using a thermal shift assay. This technique measures protein stability changes, indicated by its thermal denaturation temperature, when bound by a compound. We used purified GST-C-RAF RBD protein and analyzed its thermal denaturation temperature (dTm) in the presence of high concentration of clinical-grade rigosertib. We observed a small but reproducible increase in dTm for GST-C-RAF RBD in presence of rigosertib compared to the DMSO control (Figure S1A). However, this temperature shift was smaller than previously observed with the same assay,[12] and there was no significant increase of protein stability compared to the dTm shift measured for the GST control protein with rigosertib. Therefore, these results did not unambiguously demonstrate a significant binding of rigosertib to C-RAF RBD.

We then employed an indirect approach by testing whether rigosertib competes with active RAS for binding to C-RAF RBD using *in vitro* competition binding assays, similar to the previously published study.[12] Purified GST-C-RAF RBD immobilized on beads was pre-incubated with rigosertib or DMSO overnight and then incubated with total lysates from EGF-stimulated HeLa cells. We quantified the amount of active RAS that bound to C-RAF RBD by western blot in presence or in absence of rigosertib. If rigosertib competitively displaced RAS from C-RAF RBD binding, we would expect a decrease in active RAS pull down by the C-RAF RBD beads. However, we did not observe any change of active RAS levels in rigosertib treated samples, suggesting that in the tested conditions, rigosertib does not compete with active RAS from HeLa cell lysates for binding to purified C-RAF RBD despite concentrations as high as 50 μM (Figure S1B).

Since this experimental setting did not allow precise monitoring of the relative amounts of active RAS in the cell lysates and C-RAF RBD used for the pull-down, we modified the competition binding assay using purified $KRAS^{wt}$ loaded *in vitro* with GDP or GTPγS. Intriguingly, we did not observe any displacement of $KRAS^{wt}$-GTPγS binding to C-RAF RBD in presence of rigosertib, corroborating that rigosertib did not compete with active RAS for binding to C-RAF RBD *in vitro* (Figure S1C). We have also employed ON02180 Na (Z)-isomer as a control with the ON01910.Na (rigosertib) which is an active (E)-isomer in these assays.

Although the aforementioned results indicated that rigosertib does not act as a RAS mimetic, we sought to obtain stronger evidence utilizing a previously established NanoBiT assay to monitor RAS binding to C-RAF RBD.[20] The NanoBiT system can track the dynamics of protein-protein interaction in live cells. It is based on the split NanoLuciferase enzyme, divided into two subunits, LgBiT and SmBiT, each fused to a protein of interest. The physical interaction between these two partner proteins results in complementation to reversibly reconstitute a functional NanoLuciferase enzyme.[21] Using this NanoBiT cellular assay, we tested the effect of rigosertib on C-RAF RBD binding to the three RAS isoforms bearing the activating mutation G12V. As expected, BHK-21 cells transiently expressing the NanoBiT constructs SmBiT-C-RAF RBD and LgBiT fused to G12V mutated KRAS, HRAS, or NRAS showed a strong luminescent signal due to the intrinsic activity of these RAS G12V isoforms and their interaction with C-RAF RBD. Treatment with rocaglamide, a compound previously described to inhibit RAS activation,[22] showed a strong decrease in luminescent signal, hence

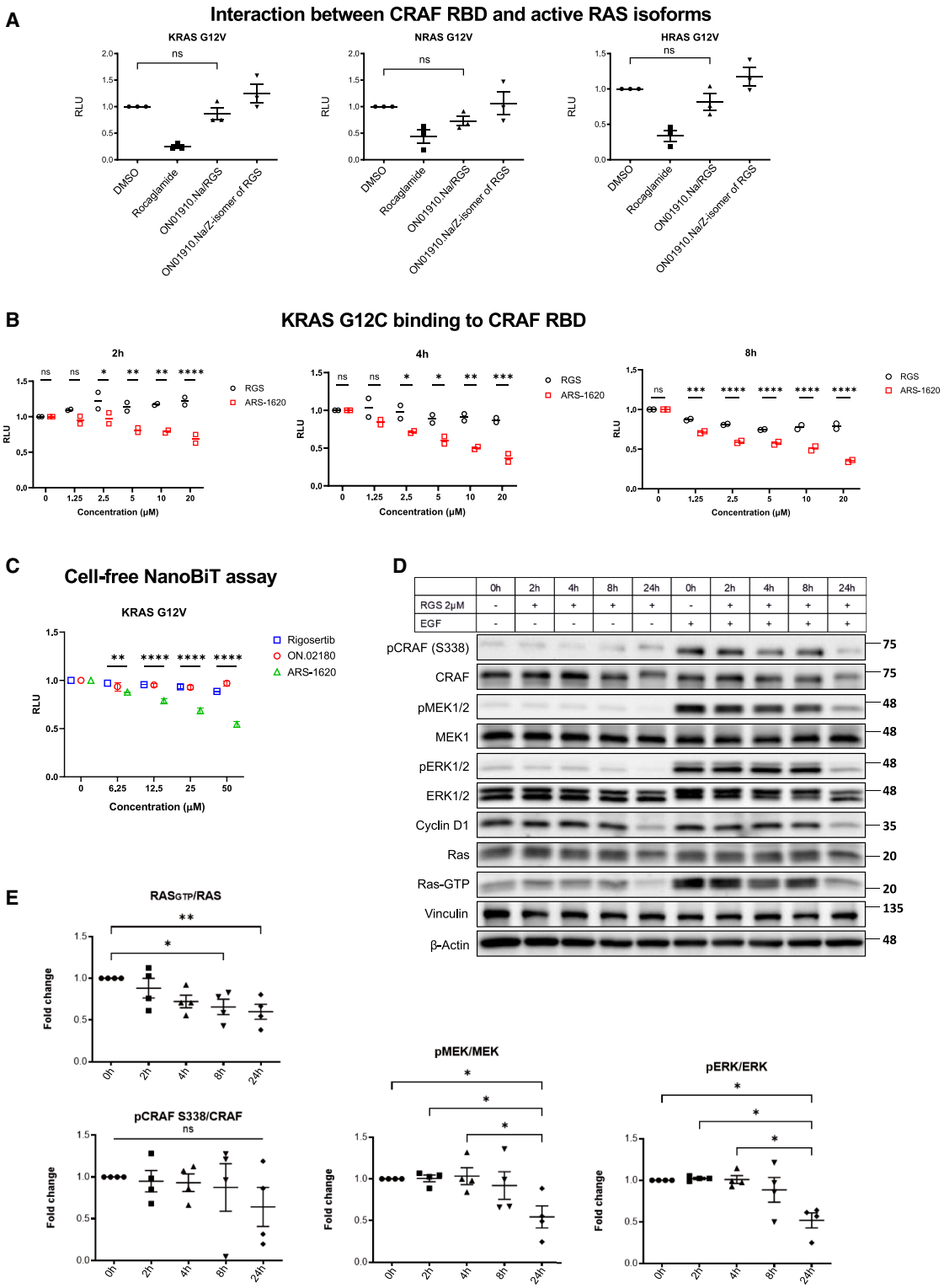

Figure 1. Rigosertib does not inhibit the interaction between active RAS with C-RAF RBD in NanoBiT assays and affects the RAS/RAF/MEK signaling pathway in HeLa cells

(A) A NanoBiT cellular assay to monitor the interaction between C-RAF RBD and active RAS. BHK-21 cells transfected with SmBiT-C-RAF RBD and the indicated LgBiT-RAS G12V construct. After 48 h, cells were treated for 8 h with DMSO, rocaglamide (Roc, 100 nM), rigosertib (20 μM) or ON02180.Na (20 μM). Shown are

(legend continued on next page)

validating the NanoBiT assay (Figure 1A). In contrast to rocaglamide, following 8 h treatment with rigosertib, we observed only a minor decrease in luminescence for all three RAS isoforms, suggesting that KRAS G12V binding to C-RAF RBD is slightly impaired in presence of rigosertib (Figure 1A).

We further compared the effect of rigosertib on RAS binding to C-RAF RBD with the G12C-specific compound ARS-1620.[23] In cells expressing SmBiT-C-RAF RBD and LgBiT-KRAS G12C, rigosertib treatment was much less potent than ARS-1620 at decreasing the luminescent signal (Figure 1B). Finally, we established a cell-free NanoBiT system using lysates of HEK-293T cells expressing SmBiT-C-RAF RBD and LgBiT-KRAS G12C or G12V. This system was validated by confirming that ARS-1620 disrupted binding of C-RAF RBD to KRAS G12C (Figure 1C). Similar to the cellular system, rigosertib did not significantly disrupt the binding of C-RAF RBD to KRAS G12C in the cell-free system.

These results are consistent with a weak binding of rigosertib to C-RAF RBD, as reported by Ritt et al..[13] Taken together, even though rigosertib binds to C-RAF RBD to some extent, our results provide evidence that this interaction was not sufficient to induce a strong displacement of RAS binding to C-RAF RBD *in vitro* or in cellular assays. Therefore, these experiments did not confirm that rigosertib acts as a RAS mimetic by binding the RBD of C-RAF.

Previous publications demonstrated an inhibition of RAS/RAF/MEK signaling after 18 h treatment with rigosertib.[12,13] The latter study also showed that this pathway was not affected by shorter treatment times. We therefore examined the effects of rigosertib on RAS/RAF/MEK signaling after 2–24 h treatment with rigosertib in HeLa cells (Figure 1D). While RAS pull-down experiments showed decreased levels of active RAS after 2–4 h treatment with rigosertib, we detected a decrease of MEK1/2 (Ser217/221),ERK1/2 (Thr202/204) phosphorylation only after longer treatment times. Phosphorylation levels tended to be lower after 8 h and showed a clear reduction after 24 h of treatment (Figures 1D, 1E, and S2). Rocaglamide served as a positive control, while the Z-isomer of rigosertib (ON02180.Na) did not show any effect on the protein expression levels. Although we could not confirm that rigosertib impairs RAS binding to its downstream effector C-RAF, our results confirmed the inhibition of RAF/MEK signaling after prolonged treatment with rigosertib.

Rigosertib activates the JNK signaling pathway

Previous work showed that rigosertib activates the stress-response kinase JNK, leading to inhibitory hyperphosphorylation of the RAS effectors C-RAF, B-RAF, and of the RasGEF SOS1.[9,13,24] This prompted us to investigate the involvement of the JNK pathway in rigosertib-mediated inhibition of RAS/RAF/MEK signaling.

In our experiments, we could affirm that 18 h treatment of HeLa cells with rigosertib led to a size shift of the bands detected by western blot for SOS1 and C-RAF, due to their hyperphosphorylation status (Figure S3A). The migration shift of C-RAF correlated to its phosphorylation on serine 642, an inhibitory post-translational modification proposed to be mediated by JNK.[13] We detected similar SOS1 and C-RAF hyperphosphorylation in cells treated with the microtubule-targeting agent colchicine. Moreover, inhibition of JNK signaling using the JNK inhibitor SP600125 led to a decrease of both rigosertib- and colchicine-induced hyperphosphorylation of SOS1 and C-RAF. Thus, consistent with previous findings, we confirmed that rigosertib treatment phenocopies the effects of mitotic stress induced by microtubule destabilization.[13] In addition, JNK inhibition partially restored phosphorylation levels of MEK1/2 and ERK1/2 after rigosertib treatment (Figures S3B and S3C), suggesting that rigosertib-mediated inhibition of RAS/RAF/MEK signaling would be at least partly dependent on the activation of JNK.

Proteome-wide CETSA MS profiling for identification of novel (off-)targets for rigosertib in intact and lysed HL60, H358, and K562 cells

In order to identify the direct targets of rigosertib in tumor cells, we performed a mass spectrometry-based cellular thermal shift assay (CETSA MS) analysis. CETSA MS is a powerful technique that identifies targets within the entire proteome engaged by chemical ligands or small molecules of interest at physiological levels in cells. This study followed the general CETSA protocol,[25] utilizing liquid chromatography-mass spectrometry (LC-MS) for detection and implementing a two concentration CETSA MS profiling strategy in the compressed format. The analysis assessed protein stability in intact or lysed cells treated with the compounds at two different concentrations relative to non-treated control cells. Treated cells/lysates were aliquoted and subjected to a heat challenge at 12 different temperatures, after which individual samples from all temperature points were pooled for each test condition. Aggregated proteins were removed by centrifugation, and soluble protein amounts were measured using LC-MS (Figure 2A). To distinguish between compound-induced protein (in)stability and protein

relative luminescence unit (RLU) values relative to DMSO control and normalized to positive control from 3 independent experiments. Data are represented as mean ± SEM. ns: not significant $p > 0.05$, (*) $p \leq 0.05$, (**) $p \leq 0.01$, (***) $p \leq 0.001$, (****) $p \leq 0.0001$.

(B) KRAS G12C binding to C-RAF RBD in a NanoBiT assay in BHK-21 cells treated 2, 4, or 8 h with increasing concentration of rigosertib. RAS G12C-binding compound ARS-1620 served as a positive control. Shown are mean RLU values for duplicates relative to DMSO control. Data are represented as a median.

(C) A cell-free NanoBiT assay in lysates of HEK-293T transfected with SmBiT-C-RAF RBD and LgBiT-KRAS G12C. Cell lysates were incubated for 4 h with increasing concentrations of ARS-1620, rigosertib or ON02180.Na. Shown are RLU values relative to DMSO control from one representative experiment out of two. Data are represented as a mean with SD. ns: not significant $p > 0.05$, (*) $p \leq 0.05$, (**) $p \leq 0.01$, (***) $p \leq 0.001$, (****) $p \leq 0.0001$.

(D) HeLa cells serum-starved and treated with rigosertib (RGS, 2 μM) for 2, 4, 8, or 24 h then stimulated with EGF at 100 ng/mL for 5 min. Active RAS pull-down and western blot analysis of pathway activation in total cell lysates. Shown is the result of one representative experiment.

(E) Quantifications of (D) for EGF-stimulated cells relative to DMSO from 4 independent experiments. Two-way ANOVA, Tukey's multiple comparisons test was used to determine significant differences. Data are represented as a mean with SEM; ns: not significant $p > 0.05$, (*) $p \leq 0.05$, (**) $p \leq 0.01$, (***) $p \leq 0.001$, (****) $p \leq 0.0001$.

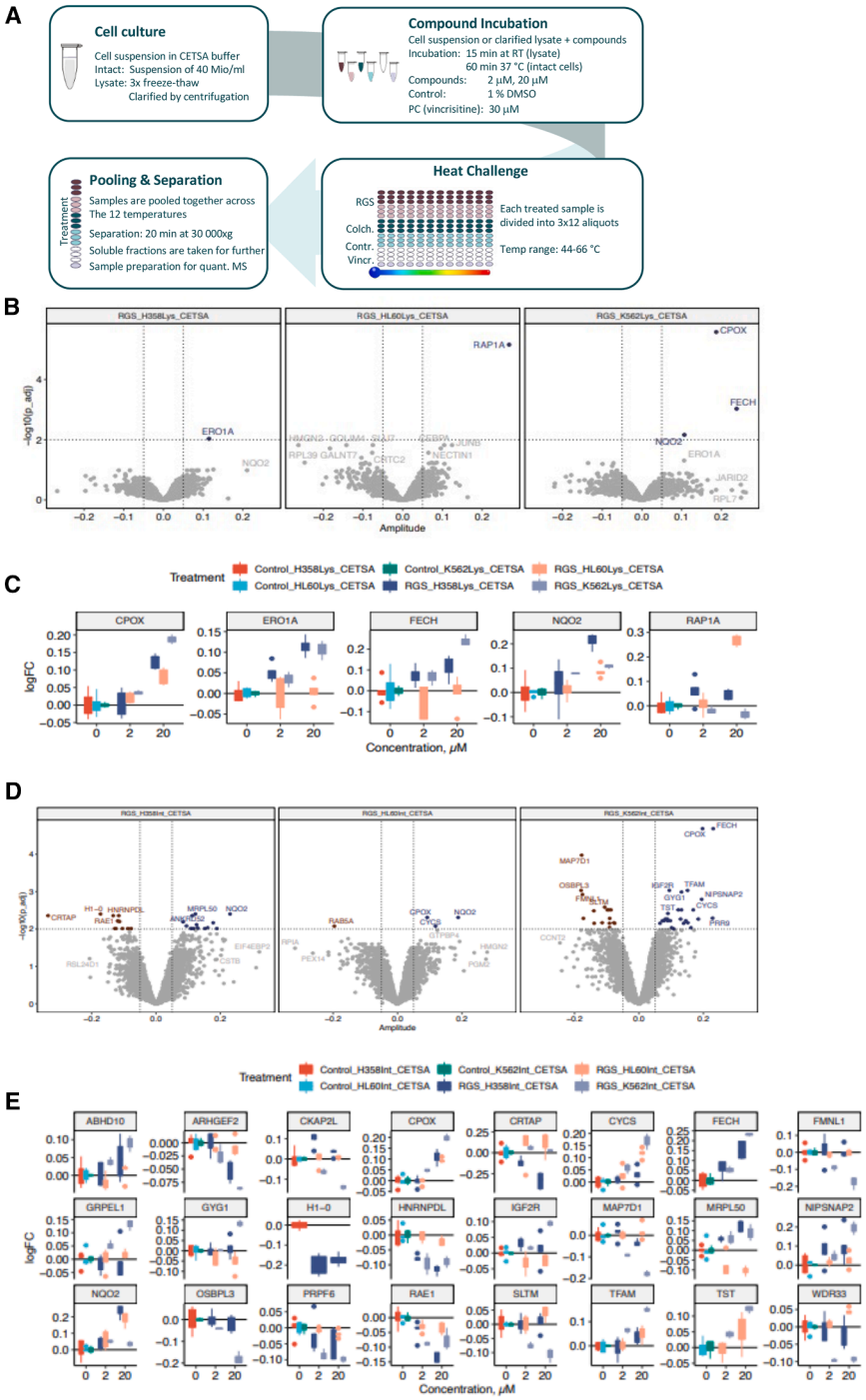

Figure 2. CETSA MS profiling of HL60, H358, and K562 cells

(A) Schematic representation of the experimental workflow of the CETSA MS assay.

(B and D) *x* axis represents effect size (amplitude, log2 fold-change), and *y* axis effect significance (−log10(pvalue)). Significance for the concentration (20 µM) response fit is based on Benjamini-Hochberg corrected *p* values from moderated t test. Only proteins with more than two tryptic peptides are shown.

(C and E) Compound-induced protein thermal stability changes after 15 min incubation of lysed HL60, H358, and K562 cells with either 2 or 20 µM of rigosertib.

abundance/solubility changes, soluble protein amounts in non-heated samples were also measured.

CETSA MS was conducted in multiple cell types to identify potential new protein targets of rigosertib across cell types. The experiments were performed in intact HL60 (acute promyelocytic leukemia), H358 (non-small lung cancer, KRAS G12C), and K562 (chronic myelogenous leukemia) cells, as well as clarified lysates of the same cells with three or five replicates for each experimental condition. Unbiased proteome-wide target engagement of rigosertib by CETSA MS profiling of cells treated with rigosertib showed no evidence of direct binding to previously suggested molecular targets such as microtubules or PLK1, or to any RBD-containing proteins (Figure S4A).

Compound-induced proteome thermal stability changes in lysed H358, HL60, and K562 cells incubated with 20 µM of rigosertib are summarized as volcano plots in Figure 2B. Here, proteins were characterized by effect size (log-transformed fold-change for the compound-treated cells relative to control) and significance (−log10-transformed *p* value from moderated t test). Only five proteins showed significant thermal stability changes in at least one out of three experiments (Figure 2C). CPOX and FECH, both from the heme synthesis pathway, appear as off-target binders for various small molecules and are, thus, unlikely to be responsible for rigosertib's pharmacology. RAP1A was also excluded from the potential targets as it was detected only in HL60 lysates treated with high rigosertib concentration. Stabilization of NQO2 (NRH:quinone oxidoreductase 2) was observed in all three cell lysates, while ERO1A (endoplasmic reticulum oxidation 1 A) was stabilized in H358 and K562 cell lysates.

Additionally, CETSA MS profiling in intact cells allowed the identification of indirectly stabilized/destabilized proteins, which could highlight events occurring downstream of rigosertib binding to its primary target(s). Compound-induced proteome thermal stability changes in intact cells incubated with 20 µM of rigosertib were summarized as volcano plots in Figure 2D. 58

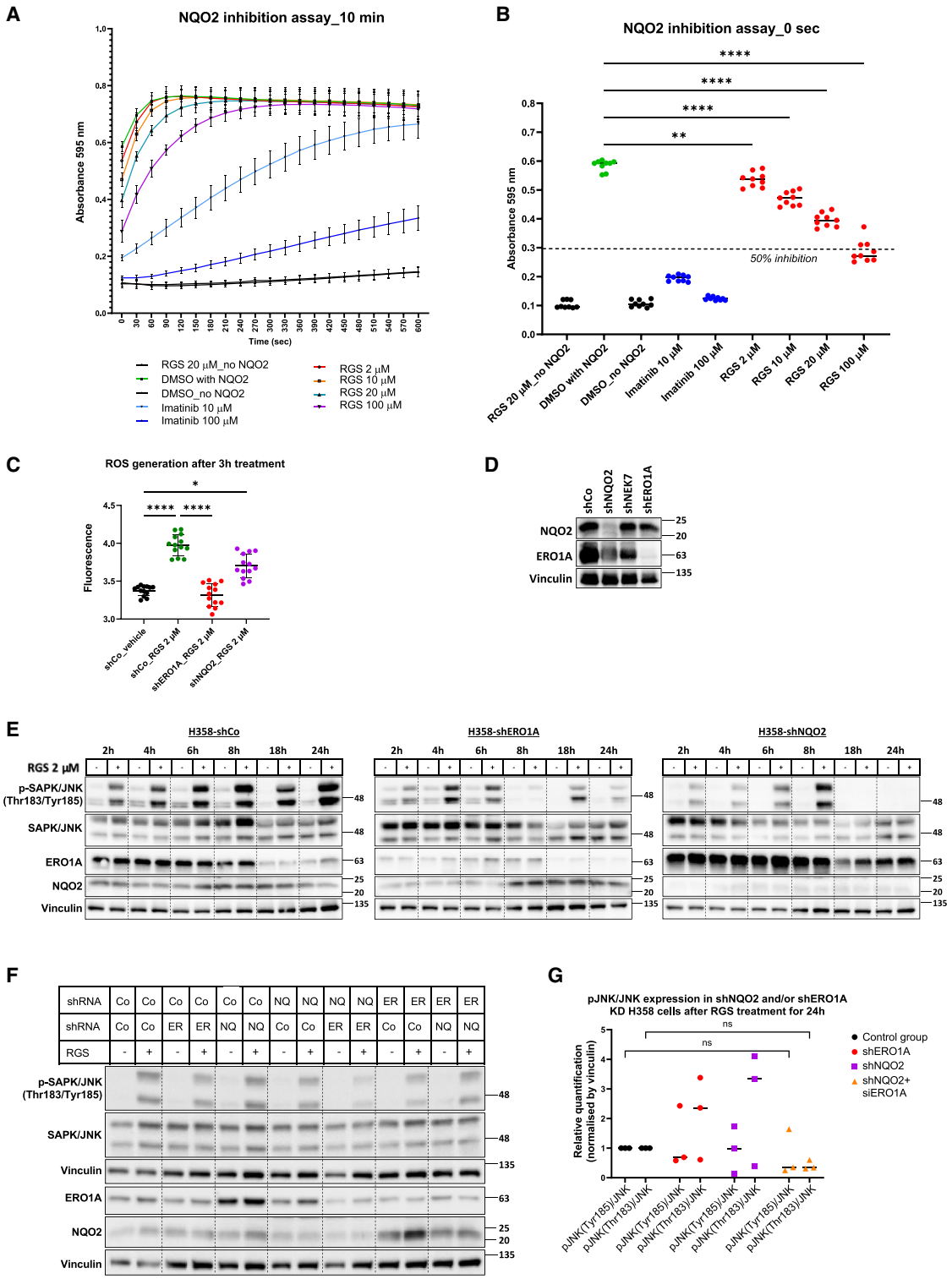

Figure 3. Rigosertib induces ROS production and activates the JNK signaling by targeting the ERO1A and NQO2

(A) Human recombinant NQO2 protein was incubated with DMSO, rigosertib (2, 10, 20, or 100 μM) and imatinib (1 or 100 μM) for 10 min. The enzymatic reactions were initiated by adding 300 μM menadione as a substrate along with 500 μM NMEH as a cosubstrate. The enzymatic activity of NQO2 was determined by measuring the absorbance at 595 nm of the reduced MTT. Data are represented as a mean with SD.

(legend continued on next page)

proteins showed significant changes in thermal stability upon incubation with 20 μM of rigosertib in at least one cell line, with 39 proteins stabilized and 29 destabilized by the compound. Figure 2E shows the 24 proteins with the most significant changes. Rigosertib-induced thermal stability changes in the three cell lines are shown for the top 24 most significant protein hits (Figure 2E). In addition to the previously observed stabilization of CPOX, FECH, and NQO2, several other proteins showed a clear concentration-dependent stabilization or destabilization. For instance, microtubule-associated proteins CKAP2L and MAP7D1 were destabilized in intact K562 cells. Among the factors identified in intact cells were also ERO1A and many mitochondria-related factors: CYCS, CPOX, FECH, NIPSNAP2, TFAM, TST, GRPEL1, ATP5PD, ACO2, and ABHD10. These results suggest that rigosertib-induced endoplasmic reticulum (ER) stress and mitochondrial stress may contribute to JNK pathway activation.

A comparison of the proteome-wide thermal stability changes in intact and lysed cells is shown in Figure S4A. Here, the CETSA amplitudes for the significantly stabilized/destabilized proteins (intact and lysate hits) are shown as a scatterplot with CETSA amplitudes from lysate on the *x* axis and from intact cells on the *y* axis. Stabilization of CPOX, FECH, and NQO2 occurs in both intact and lysed cells, ERO1A is mostly lysate-specific, and the remaining protein hits were found to shift only in intact cells. Therefore, NQO2 and ERO1A could be potential direct targets of rigosertib.

We investigated the consequences of rigosertib binding to NQO2 and ERO1A by analyzing their protein levels in H358 and HeLa cells treated with 2, 10, and 20 μM rigosertib (Figure S5A), but we did not observe significant changes in either case. However, rigosertib effectively rescued the thermal degradation of the ERO1A and NQO2 proteins (Figure S5B), indicating that these two proteins are stabilized in cells upon rigosertib treatment. We then assessed NQO2 enzymatic activity using recombinant human NQO2 protein. Various rigosertib concentrations were used (2, 10, 20, and 100 μM) to determine its inhibitory effect on NQO2 activity. Imatinib (10 and 100 μM), a known NQO2 inhibitor,[26] was used as a positive control. We detected inhibition of the NQO2 activity at higher rigosertib concentrations, indicating that rigosertib has a relatively weak but significant inhibitory effect on NQO2 enzymatic activity (Figures 3A and 3B).

A comparative analysis in K562 cells with several microtubule destabilizing agents, including rigosertib, revealed NEK7 as another potential direct target (Figure S4B). NEK7 (NIMA-related kinase 7) regulates proper spindle assembly and mitotic progression[27] and coordinates the assembly of the NLR family pyrin domain containing 3 (NLRP3) into the core of the inflammasome.[28] It should be noted that although CETSA MS profiling did not reveal PLK1 as a direct target of rigosertib, NEK7 is a downstream target of PLK1 during mitotic spindle formation as it is regulated by the PLK1-dependent NEK9 activation.[29] In addition, NEK7 shares along with PLK1, NEK6, and NEK9 a common phosphorylation-site motif, raising the possibility that these proteins can phosphorylate the same substrates.[30] This provides a plausible explanation for why rigosertib was initially described as a PLK1 inhibitor.

Although rigosertib has been proposed to directly bind to tubulin at the colchicine-binding site,[15] tubulins did not appear among the most significant targets in the CETSA MS experiments. To investigate this more rigorously, we profiled colchicine, a recognized tubulin-binding compound and classical anti-mitotic drug,[31] alongside with rigosertib in K562 cells using the same two concentrations (2 and 20 μM). Figures S4C and S4D show the scatterplot of CETSA logFC values at 20 μM of either rigosertib or colchicine in intact K562 cells. A clear colchicine-specific stabilization of several tubulins (both alpha and beta) was observed (green). Several proteins were stabilized by both colchicine and rigosertib (red) in a highly correlated manner, such as the microtubule-associated proteins CKAP2L and MAP7D1, which might indicate a similarity in the mechanism of action of the two compounds. While the CETSA MS profiles of colchicine and rigosertib were very similar in intact cells, they differed significantly in lysed K562 cells, where no common protein hits were identified. Notably, colchicine stabilized several tubulins in lysed cells, whereas rigosertib did not (Figure S4D). Thus, in the tested cell lines and experimental conditions, rigosertib does not seem to directly target tubulins, contradicting previous reports[15] and suggesting that rigosertib's effect on microtubules occurs via a different, indirect mechanism.

Rigosertib-dependent ROS generation activates JNK signaling

Studies have shown that rigosertib treatment promotes reactive oxygen species (ROS)-dependent activation of the JNK1/2 pathway.[9,13,32] To further define the events upstream of this stress signaling cascade, we investigated the roles of ERO1A and NQO2, the two ROS-related targets identified by CETSA MS. Consistent with previous studies, we detected a significant increase in ROS levels after 3 h of rigosertib treatment in H358 cells (shCo_vehicle vs. shCo_RGS 2 μM), measured by

(B) Quantification of the NQO2 enzymatic activity immediately after incubation with rigosertib or imatinib. Shown is the result of 3 experiments and ordinary one-way ANOVA, Dunnett's multiple comparisons test was used to determine significant differences.
Data are represented as a median; ns: not significant $p > 0.05$, (*) $p \leq 0.05$, (**) $p \leq 0.01$, (***) $p \leq 0.001$, (****) $p \leq 0.0001$.
(C) Quantification from 3 independent experiments of the live cell imaging of the effect of single ERO1A or NQO2 knock-down on ROS generation in H358 cells treated with rigosertib 2 μM. Significance was determined using two-way ANOVA test.
Data are represented as a mean with SD; ns: not significant $p > 0.05$, (*) $p \leq 0.05$, (**) $p \leq 0.01$, (***) $p \leq 0.001$, (****) $p \leq 0.0001$.
(D) Western blot of the lysates that were used for (C) to confirm the ERO1A and NQO2 knockdown.
(E) Western blot analysis of the effect of rigosertib on the phosphorylated JNK levels in H358-shERO1A or -shNQO2 knockdown cells from 2 to 24 h.
(F) Western blot analysis of the effect of ERO1A and NQO2 single or double knockdown in H358 cells treated with rigosertib 2 μM.
(G) Comparison of the levels of phosphorylated Thr183/Tyr185 residues of SAPK/JNK between double and single knockdown of ERO1A and NQO2 after 24 h rigosertib treatment from 3 independent experiments. Two-way ANOVA, Tukey's multiple comparisons test was used to determine significant differences.
Data are represented as a median; ns: not significant $p > 0.05$, (*) $p \leq 0.05$, (**) $p \leq 0.01$, (***) $p \leq 0.001$, (****) $p \leq 0.0001$.

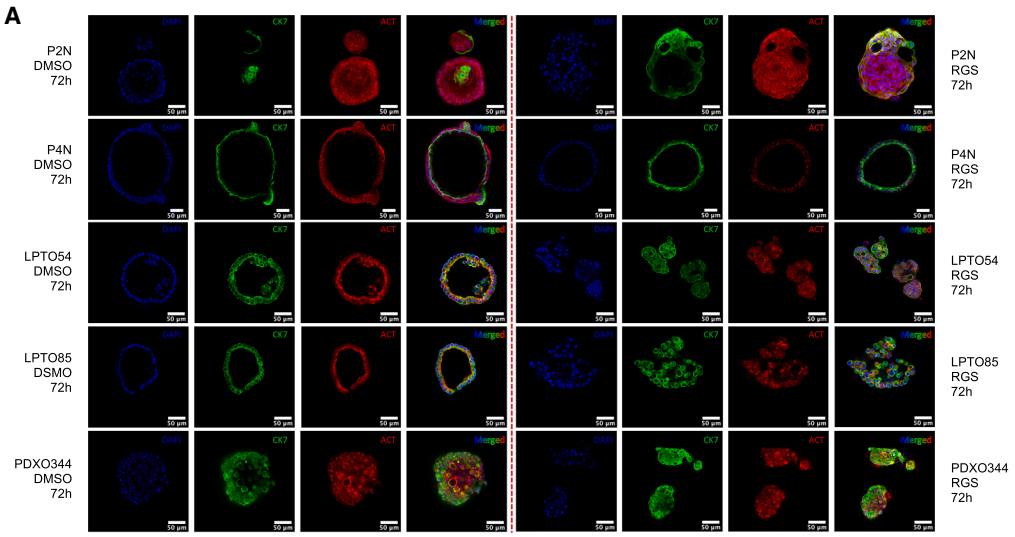

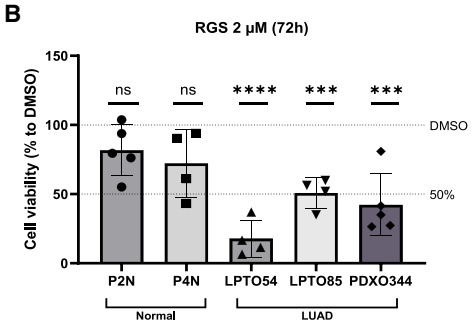

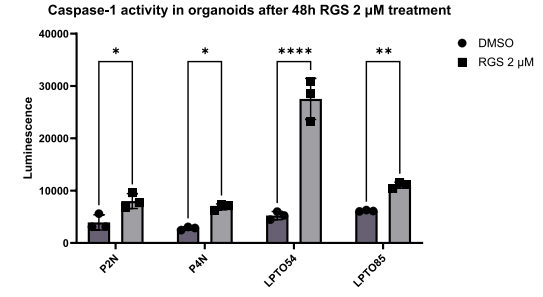

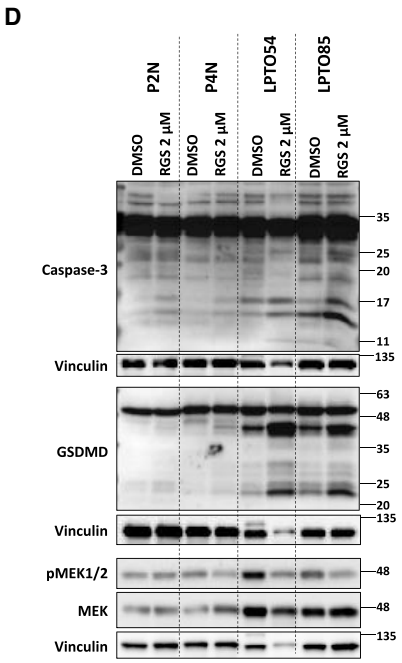

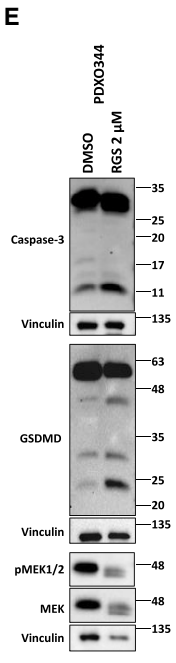

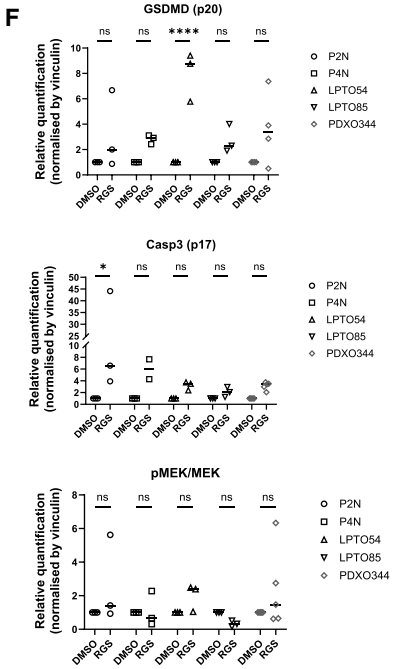

(legend on next page)

fluorescence live cell imaging using Mitotracker Green for ROS detection (Figure 3C; Videos S1, S2, S3, and S4). Importantly, ERO1A knockdown H358 cells showed reduced ROS accumulation after rigosertib treatment (shCo_RGS 2 μM vs. shERO1A_RGS 2 μM), while NQO2 knockdown cells only partially prevented the rigosertib-induced ROS generation (shCo_RGS 2 μM vs. shNQO2_RGS 2 μM) (Figure 3C; Videos S1, S2, S3, and S4). Notably, ERO1A was revealed by CETSA MS as the main target in H358 lysates treated with rigosertib 2 μM, while NQO2 was stabilized in H358 lysates and intact cells treated with higher rigosertib concentration (Figures 2C and 2E).

We next examined whether ERO1A and NQO2 influence JNK pathway activation. As expected, rigosertib treatment of H358 cells resulted in activation of c-JUN through phosphorylation of residues Thr183/Tyr185 (Figure 3E). The same experiment was performed in H358 cells with ERO1A and NQO2 knockdowns. Figure 3E shows that activation of c-JUN was partially restrained in either ERO1A or NQO2 knockdown H358 cells, indicating their role in JNK activation through oxidative stress induction. We have detected a slight increase in the protein levels of NQO2 in ERO1A knockdown cells in a cell type and passage dependent manner (Figure 3E). We then performed a double knockdown of ERO1A and NQO2 in H358 cells (Figure 3F). The decreased phosphorylated Thr183/Tyr185 residues after double ERO1A/NQO2 knockdown compared to single knockdown of these two proteins after 3 h and 24 h treatment with rigosertib (Figures S6A, S6B, and 3F), indicated that both proteins are involved in rigosertib-dependent JNK signaling activation through ROS generation. These findings suggest that ERO1A and NQO2 are the upstream targets of rigosertib that cause ROS generation leading to JNK cascade activation. However, Zhou et al. reported that the inhibition of rigosertib-mediated ROS generation did not abrogate the inhibition of RAS/MEK/ERK signaling pathway in KRAS-mutant colorectal cancer cell lines.[32]

Rigosertib's effect on microtubule polymerization

Further, we explored how rigosertib-induced cellular stress could lead to a destabilization of microtubules, since different studies have proposed that either rigosertib[15] or its contaminant impurity[33] directly bind to tubulin at the colchicine-binding site, and treatment of cells with colchicine or other microtubule destabilizing agents (MDAs) induce comparable activation of JNK and inhibition of RAS/RAF/MEK signaling.[13] To explore the hypothesis that rigosertib directly binds to tubulin, we conducted *in vitro* tubulin polymerization experiments. A concentration-dependent inhibition of tubulin polymerization by clinical-grade rigosertib was defined, showing that only high micromolar concentrations of rigosertib inhibit *in vitro* tubulin polymerization (Figures S7A and S7B). Colchicine was used as a positive control and strongly inhibited tubulin polymerization. These results confirm CETSA MS data that rigosertib has no direct effect on microtubule depolymerization at least at the relatively lower concentrations tested.

Rigosertib promotes inflammasome activation and cell death induction in patient-derived lung cancer organoids

To investigate the rigosertib-dependent cell death in cancer cells, as opposed to the low toxicity seen in normal cells,[3,32] we used three-dimensional (3D) patient-derived lung adenocarcinoma organoids (LPTOs), as well as 3D organoids established from normal tissues, which better recapitulate the biology of the patient tumor. The organoids derived from normal tissues (P2N and P4N) were developed in our lab from tissues surgically resected at Universitätsmedizin Mainz, while we also used three commercial lung adenocarcinoma organoids, which included two patient-derived organoids (LPTO54 and LPTO85) and a PDX-derived organoid (PDXO344). LPTO54 contains wt KRAS, whereas LPTO85 and PDXO344 harbor KRAS G12D or G12C mutation, respectively,[34] which both result in the activation of KRAS. To characterize the 3D organoids, we firstly examined the expression of a key lung adenocarcinoma marker, the luminal epithelial marker cytokeratin 7 (CK7), as well as the ciliated cell marker acetylated alpha-tubulin (Ac-Tub) (Figure 4A). All organoids expressed both CK7 and acetylated alpha-tubulin, confirming their epithelial origin. In addition, the organoids were stained with the fluorescent dye 4′,6-diamidino-2-phenylindole (DAPI) to determine the number of nuclei and to assess cell morphology. Based on the fluorescence intensity of DAPI signal, nuclei seemed to be more spread in rigosertib-treated cancer organoids compared to the vehicle group, indicating the loss of organoid (3D) formation due to the induction of cell death in rigosertib-treated organoids.

Figure 4. Rigosertib promotes cell death induction and caspase-1 activity to trigger IL-18 secretion in patient-derived lung cancer organoids

(A) Fluorescent staining of the expression of the luminal epithelial marker cytokeratin 7 (CK7), the lung ciliated cell marker acetylated alpha-tubulin (Ac-Tub), and nuclei (DAPI) of organoids derived from human lung cancer organoids (LPTO54, LPTO85-KRAS G12D, and PDXO344-KRAS G12C) and normal (P2N and P4N). Organoids were treated with DMSO or RGS 2 μM for 72 h.

(B) Cell viability of organoids derived from human lung cancer organoids (LPTO54, LPTO85, and PDXO344) and normal (P2N and P4N) after 72 h rigosertib treatment. Ordinary one-way ANOVA, Tukey's multiple comparisons test was used to determine significant differences.

Data are represented as a mean with SD; ns: not significant $p > 0.05$, (*) $p \leq 0.05$, (**) $p \leq 0.01$, (***) $p \leq 0.001$, (****) $p \leq 0.0001$.

(C) Analysis of NLRP3 inflammasome activation marker caspase-1 after 48 h rigosertib treatment of the organoids. Two-way ANOVA, Šídák's multiple comparisons test was used to determine significant differences.

Data are represented as a mean with SD; ns: not significant $p > 0.05$, (*) $p \leq 0.05$, (**) $p \leq 0.01$, (***) $p \leq 0.001$, (****) $p \leq 0.0001$.

(D and E) Western blot analysis of cell death activation markers after 72 h rigosertib treatment of organoids. Vinculin levels are detected as a loading control for each blot and presented below. Activation of pyroptotic death was measured by immunoblotting of activated GSDMD (p20). Activation of apoptosis was measured by immunoblotting of active caspase-3 (p17).

(F) Quantification of (D and E) from 3 independent experiments. Two-way ANOVA, Tukey's multiple comparisons test was used to determine significant differences.

Data are represented as a median; ns: not significant $p > 0.05$, (*) $p \leq 0.05$, (**) $p \leq 0.01$, (***) $p \leq 0.001$, (****) $p \leq 0.0001$.

We further determined the rigosertib effect on cell death initiation in the patient-derived lung cancer organoids using the the CellTiter-Glo3D assay. Rigosertib reduced the cell viability of both normal and cancerous organoids (Figure 4B). However, organoids from the KRAS wild-type patient (LPTO54) showed a significantly greater reduction ($p \leq 0.0001$) in cell viability after 72 h of rigosertib treatment. Importantly, rigosertib also decreased the viability of the LPTO85 (KRAS G12D) ($p \leq$ 0,001) and PDXO344 (KRAS G12C) ($p \leq 0,001$) organoids by at least 50% (Figure 4B). Supporting these findings, widefield microscopy demonstrated rigosertib-induced loss of membrane integrity in LPTO54 organoids compared to the control organoids after 72 h (Videos S5 and S6). Both LPTO54 and PDXO344 patients are positive to the lung adenocarcinoma prognostic marker thyroid transcription factor 1 (TTF-1) based on organoid immunohistochemistry (IHC) data and were classified as stage 1A. Meanwhile, LPTO85 were TTF-1 negative and classified as stage 1B.[34] TTF-1 positivity in lung adenocarcinoma is associated with better progression-free survival (PFS) and overall survival than in TTF-1 negative groups.[35] This may explain the higher sensitivity of LPTO54 (TTF-1+, stage 1A, $KRAS^{wt}$) and PDXO344 (TTF-1 focal, stage 1A, KRAS G12C) organoids to rigosertib treatment compared to LPTO85 (TTF-1-, stage 1B, KRAS G12D) organoids.

Recent studies described a rigosertib-dependent immunogenic cell death induction in colorectal cancer,[16] as well as enhanced inflammatory cytokines secretion in colon cancer.[36] The NLRP3 inflammasome is considered a critical component of the innate immunity that is responsible for pyropoptic cell death and proinflammatory cytokines secretion.[37,38] However, its diverse roles across different tumor types are still a challenging topic in terms of treatment strategies.[39] Given the emerging evidence that ROS can activate the NLRP3 inflammasome,[40] as well as the necessity of NEK7 for NLRP3 assembly and activation,[41] we investigated whether NLRP3 inflammasome activation could be a consequence of rigosertib treatment. Upon inflammasome stimulation, the apoptosis-associated speck-like protein containing a caspase recruitment domain (ASC) facilitates the recruitment of caspase-1 to the NLRP3 complex. Caspase-1 is a cysteine protease that cleaves the pyroptosis-mediator gasdermin (GSDMD) into two fragments.[42–44] The GSDMD N terminus oligomerizes in membranes to form pores, allowing the secretion of the proinflammatory cytokines interleukin-1β (IL-1β) and interleukin-18 (IL-18).[42,45] Thus, we assessed the effect of rigosertib treatment on the release of proinflammatory cytokines and activation of inflammatory cell death. The initiation of pyroptosis was monitored by a caspase-1 activity ELISA assay using the cell supernatant. As expected, caspase-1 activity was significantly increased after 48 h of rigosertib treatment in LPTO54 ($p \leq 0.0001$) and LPTO85 ($p \leq 0,01$) organoids, while there were significantly lower changes in caspase-1 activity observed in normal P2N and P4N organoids ($p \leq 0,05$) (Figure 4C).

Cell viability and inflammatory responses were further validated biochemically by protein expression levels of apoptosis (cleaved caspase-3) and pyroptosis (cleaved GSDMD) mediators. Rigosertib treatment (2 μM, 72 h) did not lead to any significant caspase-3 activation in either normal or cancerous organoids (Figures 4D and 4F, upper panel). In contrast, GSDMD cleavage (p20) was significantly increased in LPTO54, aligning well with the activity profile of caspase-1 (Figure 4C). These data suggest that rigosertib-induced cell death in LPTO54 is likely executed by pyroptosis, while pathways other than pyroptosis and caspase-3-mediated apoptosis seem to be responsible for cell death observed in LPTO85 and PDXO344.

Rigosertib activates NLRP3 inflammasome in THP1 cells

To further investigate the role of rigosertib on the NLRP3 inflammasome, we made use of THP1 (human monocytic cell line derived from an acute monocytic leukemia patient) cells, a common model to study monocyte/macrophage functions.[46] THP1 monocytes were differentiated to macrophages by phorbol 12-myristate-13-acetate (PMA), and immune responses were stimulated by lipopolysaccharide (LPS). Consistent with our data obtained from lung cancer organoids, rigosertib treatment resulted in a significant activation of inflammatory responses. Caspase-1 activity was significantly increased upon rigosertib treatment of THP1 monocytes (Figure S8A). As expected after LPS treatment, both THP1 monocytes and macrophages showed elevated caspase-1 activity, while the addition of rigosertib in THP1 macrophages, significantly raised the caspase-1 activity levels. Besides, significantly higher IL-1β levels were detected by ELISA in the macrophages supernatants, after treatment with rigosertib (Figure S8B). Meanwhile, significantly higher IL-18 levels were detected in the rigosertib-treated macrophages after LPS stimulation (Figure S8C). Thus, the IL-18 and IL-1β rates are assumed to be a cell type-dependent factor. To further corroborate the involvement of the NLRP3 inflammasome in rigosertib-induced caspase-1 activation, we used bone marrow-derived macrophages (BMDMs) as a second model system. Infected BMDMs derived from mice were lacking key molecules (Nlrp3−/− or Asc−/−) involved in the activation of NLRP3 inflammasome dependent cell death.[47] Whereas 18 h rigosertib treatment (2 μM) lead to clear induction of caspase-1 activity in the BMDMs derived from the wild-type mice; knockdown of either NLRP3 or ASC prevented caspase-1 activation (Figure S8D). The data presented herein confirm the rigosertib-dependent stimulation of inflammation and show the activation of caspase-1 through inflammasome assembly and consequent secretion of IL-1β and IL-18, which seems to be cell type dependent.

DISCUSSION

This study employed *in vitro* binding assays and competition experiments in HeLa and BHK-21 cells, revealing that rigosertib does not directly displace RAS from its RBD-containing effectors, indicating it does not function as a RAS mimetic. However, our experiments confirm that rigosertib inhibits EGF-induced RAS/RAF/MEK signaling after 18 h of treatment in serum-starved HeLa cells. It remains to be determined what causes the inhibition of RAS after only 2 h of rigosertib treatment and why the inhibition of its downstream effectors is ‘‘delayed’’ by several hours.

While rigosertib’s inhibition of RAS/RAF/MEK signaling contributes to its antitumor activity, its upstream target(s) remained

unknown for years. To unravel its mechanism of action, we performed compressed CETSA MS profiling in intact HL60, H358, and K562 cells, along with their lysates. The analysis quantified more than 7,000 protein groups, representing a large portion of the soluble proteome. Only a few proteins showed clear and consistent rigosertib-induced thermal stability changes across different matrices. Among these were the ferrochelatase FECH and the oxygen-dependent coproporphyrinogen-III oxidase CPOX, both involved in the heme synthesis pathway. However, since both FECH and CPOX are common off-target binders for small molecules, they are unlikely to be responsible for rigosertib's pharmacological effects. We also observed the stabilization of NQO2 and ERO1A in lysed cells. ERO1A is induced under persistent endoplasmic reticulum stress and is implicated in the generation of ROS.[48] NQO2 produces ROS when derailed from its normal function by inhibitors or structural damage (direct)[49,50] and as deleterious byproduct of its normal activity (indirect).[51] Studies have highlighted the role of elevated ROS in activating signaling pathways, including the JNK cascade, resulting in cell death.[52,53] Interestingly, a recent study suggested that targeting of NQO2 with curcumol in NSCLC cells induces ROS/ER stress and JNK pathway activation and sensitizes cancer cells to apoptosis.[50] Collectively, these results support the proposed mechanism whereby rigosertib induces oxidative stress.

To characterize rigosertib's anti-tumor effect on the RAS/RAF/MEK signaling pathway, we examined the model proposed by Ritt et al., which suggests that rigosertib indirectly inhibits MAPK signaling via an oxidative stress-mediated phospho-regulatory circuit.[13] Our data align with this mechanism, where rigosertib-mediated stabilization, primarily of ERO1A and to a lesser extent NQO2, leads to ROS production and downstream activation of c-JUN. This results in the inhibitory hyperphosphorylation of key components of the stress signaling pathway, such as C-RAF. However, our data is also in line with Günther et al., who suggested that rigosertib-induced ROS production leads to DNA damage and cell death through JNK activation in breast and prostate cancer cells.[54] Recently, researchers confirmed both RAS/MEK/ERK signaling inhibition and ROS generation in rigosertib-treated colorectal cancer cells, though these effects were independent of each other.[32]

Beyond JNK activation, rigosertib was proposed to directly bind to tubulin acting as a microtubule destabilizing agent.[15] However, CETSA MS profiling did not show any direct binding of rigosertib to either tubulins or PLK1 kinase at concentrations up to 30 μM. Moreover, our experiments demonstrated that rigosertib can directly inhibit tubulin polymerization *in vitro* but only at high concentrations (>50 μM). Nonetheless, indirect perturbation of microtubules was observed in intact K562 cells, as evidenced by the destabilization of MAP7D1 and CKAP2L. Comparative analysis of known microtubule destabilizing compounds revealed NEK7 as another potential direct target of rigosertib. Remarkably, CETSA MS profiling revealed that rigosertib displayed similar sensitivity patterns on NEK7 as several microtubule disruptors, like vincristine, vinblastine, and vinorelbine, indicating its relevance to tubulin depolymerization. PLK1, which plays a role in spindle assembly and microtubule-kinetochore attachment, was reported to activate NEK7, which may explain why rigosertib was initially described as PLK1 inhibitor. Moreover, rigosertib and colchicine, a known microtubule destabilizer, induced a strikingly similar pattern of changes in the thermal stability of the proteome in intact K562 cells, suggesting a similar mechanism of action.

Since several reports describe the modulation of proinflammatory cytokines by rigosertib,[16,18,19,36] we investigated its effect on the inflammatory response using lung cancer and normal organoids as *in vitro* cancer models. Thanks to their 3D architecture, organoids offer unique properties for the preclinical investigation of oncogenic processes that are difficult to study in traditional *in vitro* systems. We observed limited viability of the rigosertib-treated organoids derived from lung adenocarcinoma patients, while organoids derived from normal tissues showed little cytotoxicity after treatment. We further assessed the activation/cleavage of GSDMD, caspase-1, and caspase-3 to determine the induction of pyroptosis and apoptosis in lung cancer organoids compared to normal ones. We observed robust induction of pyroptosis in LPTO54 organoids (wild-type RAS) as evidenced by significantly increased GSDMD cleavage and inflammatory caspase-1 activity in the cell supernatants of rigosertib-treated cancer organoids, while (caspase-3-dependent) apoptosis was not activated in any of the tested organoids. We expedited these findings by examining the effect of rigosertib on THP1 cells, demonstrating that rigosertib activates caspase-1 and triggers IL-1β and/or IL-18 secretion. It remains to be determined which type of cell death pathway causes the reduced viability of rigosertib-treated PDXO344 (KRAS G12C) and LPTO85 (KRAS G12D). Notably, we did not observe a significant change in MEK1/2 phosphorylation in any of the rigosertib-treated organoids suggesting that reduced MAPK signaling does not contribute significantly to the cell death observed in these organoids. This contrasts with previous observations in rigosertib-treated cell lines, likely reflecting the more complex and physiologically relevant architecture of organoids. Collectively, our data suggest that rigosertib is a multi-kinase inhibitor, which elicits its anti-tumor properties in a context-dependent manner through engagement of different pathways to induce cell death.

Although challenges remain in combining anticancer treatments with pyroptotic-inducing strategies, an increasing number of studies have found a variety of drugs, including the chemotherapeutics doxorubicin, paclitaxel, cisplatin, 5-FU etc., which can elicit tumor cell death by inducing pyroptosis.[55–60] Given the established role of inflammation in cancer development, regulation, and response to therapy,[61,62] the observed rigosertib-induced inflammatory signatures may enhance its anti-tumor efficacy by supporting the conversion of "cold" to "hot" tumors,[63] a common hallmark of successful tumor treatment with immunomodulatory agents. This effect may provide significant clinical benefits in patients with NSCLC and other diseases by enhancing the effectiveness of different treatment strategies.

Overall, our study provides deeper insights into the mechanisms of action of rigosertib, highlighing cell type- and concentration-dependent modes of action. Rigosertib appears to be an effective compound for inhibition of RAS/RAF/MEK signaling, partially mediated by the engagement of ERO1A and NQO2 proteins, which drive ROS-dependent JNK activation in certain tumor and cell types. Depending on the tumor/cell/organoid

type, however, inhibition of the oncogenic pathway may not depend on JNK activation (H358 cells, colorectal cancer cells[17]). Moreover, rigosertib's ability to modulate the inflammatory responses suggests a reprogramming of the tumor immune environment, which may contribute to the synergistic effect seen with immune checkpoint inhibitors in both preclinical and clinical settings. These findings support rigosertib's promise as a multifaceted therapeutic agent, particularly in cancer treatments involving immune modulation.

Limitations of the study

In this manuscript, we have primarily investigated two targets of RGS that are relevant to ROS production, despite the fact that multiple targets have been identified in a cell type- and concentration-dependent manner. While our focus is on these two targets, we cannot rule out the possibility that other targets may also contribute to RGS's mechanism of action. Additionally, we show that at higher concentrations, RGS may act as a tubulin disruptor; however, it is uncertain whether such concentrations are achievable under clinical treatment conditions.

The experimental models used in this study did not account for sex- or gender-specific effects. Currently, there is no evidence suggesting that sex or gender influences the outcomes observed. However, the majority of research to date has focused on rigosertib's general efficacy and mechanisms of action across various cancer types, with limited attention to potential sex- or gender-related differences. This represents a limitation of the present study as well.

RESOURCE AVAILABILITY

Lead contact

Further information and requests for resources and reagents should be directed to and will be fulfilled by the lead contact, Krishnaraj Rajalingam (krishna@uni-mainz.de).

Materials availability

This study did not generate new unique reagents.

Data and code availability

- Data: CETSA-MS data have been deposited at Zenodo and are publicly available as of the date of publication. The accession number is listed in the key resources table.
- Code: The study did not generate new code.
- Other items: Original western blot images have been deposited at Zenodo. The accession number is listed in the key resources table. Any additional information required to reanalyze the data reported in this paper is available from the lead contact upon request.

ACKNOWLEDGMENTS

The graphical abstract was drawn using Biorender.com.

This work was supported by the subproject TP05 of CRC1292 funded by the Deutsche Forschungsgemeinschaft (DFG), Germany.

AUTHOR CONTRIBUTIONS

P.K., H.Y., C.D., R.R., S.C., and S.M.F. contributed to the conceptualization, performed experiments, data curation, and analysis. A.C. contributed to the CETSA analysis. G.H. performed microscopy analysis. M.O. provided technical support. K.R. contributed to the design, analysis and supervision of the projet. P.K. and K.R. wrote the manuscript with inputs from all authors.

DECLARATION OF INTERESTS

K.R. is the founder and managing director of KHR biotech GmbH, SJP Biotec GmbH, and KRAS Research GmbH and has served as a consultant for Onconova therapeutics in the past. S.M.F. and S.C. were employees of Onconova therapeutics (now TRAWS pharma). A.C. is an employee of PelagoBioSciences.

STAR★METHODS

Detailed methods are provided in the online version of this paper and include the following:

- KEY RESOURCES TABLE
- EXPERIMENTAL MODEL AND STUDY PARTICIPANT DETAILS
  - Cell lines
  - Human tissue material
  - Bone marrow derived macrophages (BMDMs)
- METHOD DETAILS
  - Thermal shift assay
  - Competition assay for binding to C-RAF-RBD
  - NanoBiT assay
  - Active RAS pulldown
  - SDS-PAGE and western blotting
  - Antibodies
  - *In vitro* tubulin polymerization
  - NQO2 enzymatic activity assay
  - Thermal shift assay
  - Lentiviral-mediated knockdown of CETSA MS revealed targets
  - siRNA transfection
  - Transient transfections of stably transfected cells
  - Enzyme-linked immunosorbent assay (ELISA)
  - Caspase-1 activity
  - Live-cell imaging and cell tracking analyses
  - Organoid derivation from lung tissue
  - Culture of lung normal and 3dGRO LUAD human organoids
  - Immunofluorescence staining, clearing and image acquisition of organoids
  - Cell viability assay Glo 3D
  - Live cell imaging of organoids
  - CETSA
  - Compounds
  - Compressed CETSA MS experiment
  - Protein digestion and labeling
  - LC-MS/MS analysis
  - Protein identification
- QUANTIFICATION AND STATISTICAL ANALYSIS
  - Quantification and statistical analysis LC-MS/MS
  - Quantification and statistical analyses immunoblots
  - Statistical analyses NanoBit-Assays

SUPPLEMENTAL INFORMATION

Supplemental information can be found online at https://doi.org/10.1016/j.isci.2025.112748.

Received: November 5, 2024
Revised: March 22, 2025
Accepted: May 22, 2025
Published: May 26, 2025

REFERENCES

1. Reddy, M.V.R., Mallireddigari, M.R., Cosenza, S.C., Pallela, V.R., Iqbal, N. M., Robell, K.A., Kang, A.D., and Reddy, E.P. (2008). Design, synthesis, and biological evaluation of (*E*)-styrylbenzylsulfones as novel anticancer agents. J. Med. Chem. *51*, 86–100. https://doi.org/10.1021/jm701077b.

2. Gumireddy, K., Reddy, M.V.R., Cosenza, S.C., Boominathan, R., Baker, S. J., Papathi, N., Jiang, J., Holland, J., and Reddy, E.P. (2005). ON01910, a non-ATP-competitive small molecule inhibitor of Plk1, is a potent anticancer agent. Cancer Cell *7*, 275–286. https://doi.org/10.1016/j.ccr.2005.02.009.

3. Reddy, M.V.R., Venkatapuram, P., Mallireddigari, M.R., Pallela, V.R., Cosenza, S.C., Robell, K.A., Akula, B., Hoffman, B.S., and Reddy, E.P. (2011). Discovery of a Clinical Stage Multi-Kinase Inhibitor Sodium (E)-2-{2-methoxy-5-[(2',4',6'-trimethoxystyrylsulfonyl)methyl]phenylamino}acetate (ON 01910.Na): Synthesis, Structure–Activity Relationship, and Biological Activity. J. Med. Chem. *54*, 6254–6276. https://doi.org/10.1021/jm200570p.

4. Atanasova, V.S., Pourreyron, C., Farshchian, M., Lawler, M., Brown, C.A., Watt, S.A., Wright, S., Warkala, M., Guttmann-Gruber, C., Hofbauer, J.P., et al. (2019). Identification of Rigosertib for the Treatment of Recessive Dystrophic Epidermolysis Bullosa–Associated Squamous Cell Carcinoma. Clin. Cancer Res. *25*, 3384–3391. https://doi.org/10.1158/1078-0432.ccr-18-2661.

5. Ma, H., Nie, C., Chen, Y., Li, J., Xie, Y., Tang, Z., Gao, Y., Ai, S., Mao, Y., Sun, Q., and Lu, R. (2021). Therapeutic Targeting PLK1 by ON-01910.Na Is Effective in Local Treatment of Retinoblastoma. Oncol. Res. *28*, 745–761. https://doi.org/10.3727/096504021x16130322409507.

6. Vulin, M., Jehanno, C., Sethi, A., Correia, A.L., Obradović, M.M.S., Couto, J.P., Coissieux, M.-M., Diepenbruck, M., Preca, B.-T., Volkmann, K., et al. (2022). A high-throughput drug screen reveals means to differentiate triple-negative breast cancer. Oncogene *41*, 4459–4473. https://doi.org/10.1038/s41388-022-02429-0.

7. Steegmaier, M., Hoffmann, M., Baum, A., Lénárt, P., Petronczki, M., Krssák, M., Gürtler, U., Garin-Chesa, P., Lieb, S., Quant, J., et al. (2007). BI 2536, a Potent and Selective Inhibitor of Polo-like Kinase 1, Inhibits Tumor Growth In Vivo. Curr. Biol. *17*, 316–322. https://doi.org/10.1016/j.cub.2006.12.037.

8. Prasad, A., Park, I.W., Allen, H., Zhang, X., Reddy, M.V.R., Boominathan, R., Reddy, E.P., and Groopman, J.E. (2009). Styryl sulfonyl compounds inhibit translation of cyclin D1 in mantle cell lymphoma cells. Oncogene *28*, 1518–1528. https://doi.org/10.1038/onc.2008.502.

9. Chapman, C.M., Sun, X., Roschewski, M., Aue, G., Farooqui, M., Stennett, L., Gibellini, F., Arthur, D., Pérez-Galán, P., and Wiestner, A. (2012). ON 01910.Na Is Selectively Cytotoxic for Chronic Lymphocytic Leukemia Cells through a Dual Mechanism of Action Involving PI3K/AKT Inhibition and Induction of Oxidative Stress. Clin. Cancer Res. *18*, 1979–1991. https://doi.org/10.1158/1078-0432.ccr-11-2113.

10. Anderson, R.T., Keysar, S.B., Bowles, D.W., Glogowska, M.J., Astling, D. P., Morton, J.J., Le, P., Umpierrez, A., Eagles-Soukup, J., Gan, G.N., et al. (2013). The Dual Pathway Inhibitor Rigosertib Is Effective in Direct Patient Tumor Xenografts of Head and Neck Squamous Cell Carcinomas. Mol. Cancer Ther. *12*, 1994–2005. https://doi.org/10.1158/1535-7163.mct-13-0206.

11. Prasad, A., Khudaynazar, N., Tantravahi, R.V., Gillum, A.M., and Hoffman, B.S. (2016). ON 01910.Na (rigosertib) inhibits PI3K/Akt pathway and activates oxidative stress signals in head and neck cancer cell lines. Oncotarget *7*, 79388–79400. https://doi.org/10.18632/oncotarget.12692.

12. Sai, R., Dutta, K., Stacey, S., Basu, I., Yogesh, M.V., Ueno, L., and Jonathan. (2016). A Small Molecule RAS-Mimetic Disrupts RAS Association with Effector Proteins to Block Signaling. Cell *165*, 643–655. https://doi.org/10.1016/j.cell.2016.03.045.

13. Ritt, D.A., Abreu-Blanco, M.T., Bindu, L., Durrant, D.E., Zhou, M., Specht, S.I., Stephen, A.G., Holderfield, M., and Morrison, D.K. (2016). Inhibition of Ras/Raf/MEK/ERK Pathway Signaling by a Stress-Induced Phospho-Regulatory Circuit. Mol. Cell *64*, 875–887. https://doi.org/10.1016/j.molcel.2016.10.029.

14. Liu, Z., Wang, M., Wang, H., Fang, L., and Gou, S. (2020). Targeting RAS-RAF pathway significantly improves antitumor activity of Rigosertib-derived platinum(IV) complexes and overcomes cisplatin resistance. Eur. J. Med. Chem. *194*, 112269. https://doi.org/10.1016/j.ejmech.2020.112269.

15. Jost, M., Chen, Y., Gilbert, L.A., Horlbeck, M.A., Krenning, L., Menchon, G., Rai, A., Cho, M.Y., Stern, J.J., Prota, A.E., et al. (2017). Combined CRISPRi/a-Based Chemical Genetic Screens Reveal that Rigosertib Is a Microtubule-Destabilizing Agent. Mol. Cell *68*, 210–223.e6. https://doi.org/10.1016/j.molcel.2017.09.012.

16. Yan, C., Saleh, N., Yang, J., Nebhan, C.A., Vilgelm, A.E., Reddy, E.P., Roland, J.T., Johnson, D.B., Chen, S.-C., Shattuck-Brandt, R.L., et al. (2021). Novel induction of CD40 expression by tumor cells with RAS/RAF/PI3K pathway inhibition augments response to checkpoint blockade. Mol. Cancer *20*, 85. https://doi.org/10.1186/s12943-021-01366-y.

17. Zhou, X., Fu, D., Yang, H., Le, C., Lu, Y., Wei, J., Tang, Y., Zhang, J., Yuan, Y., Ding, K., and Xiao, Q. (2023). Rigosertib promotes anti-tumor immunity via autophagic degradation of PD-L1 in colorectal cancer cells. Cancer Lett. *577*, 216422. https://doi.org/10.1016/j.canlet.2023.216422.

18. Rahmani, F., Asgharzadeh, F., Avan, A., Barneh, F., Parizadeh, M.R., Ferns, G.A., Ryzhikov, M., Ahmadian, M.R., Giovannetti, E., Jafari, M., et al. (2020). Rigosertib potently protects against colitis-associated intestinal fibrosis and inflammation by regulating PI3K/AKT and NF-κB signaling pathways. Life Sci. *249*, 117470. https://doi.org/10.1016/j.lfs.2020.117470.

19. Wang, Y., Du, P., and Jiang, D. (2021). Rigosertib inhibits MEK1–ERK pathway and alleviates lipopolysaccharide-induced sepsis. Immun. Inflamm. Dis. *9*, 991–999. https://doi.org/10.1002/iid3.458.

20. Yurugi, H., Zhuang, Y., Siddiqui, F.A., Liang, H., Rosigkeit, S., Zeng, Y., Abou-Hamdan, H., Bockamp, E., Zhou, Y., Abankwa, D., et al. (2020). A subset of flavaglines inhibits KRAS nanoclustering and activation. J. Cell Sci. *133*, jcs244111. https://doi.org/10.1242/jcs.244111.

21. Dixon, A.S., Schwinn, M.K., Hall, M.P., Zimmerman, K., Otto, P., Lubben, T.H., Butler, B.L., Binkowski, B.F., Machleidt, T., Kirkland, T.A., et al. (2016). NanoLuc Complementation Reporter Optimized for Accurate Measurement of Protein Interactions in Cells. ACS Chem. Biol. *11*, 400–408. https://doi.org/10.1021/acschembio.5b00753.

22. Yurugi, H., Marini, F., Weber, C., David, K., Zhao, Q., Binder, H., Désaubry, L., and Rajalingam, K. (2017). Targeting prohibitins with chemical ligands inhibits KRAS-mediated lung tumours. Oncogene *36*, 4778–4789. https://doi.org/10.1038/onc.2017.93.

23. Janes, M.R., Zhang, J., Li, L.-S., Hansen, R., Peters, U., Guo, X., Chen, Y., Babbar, A., Firdaus, S.J., Darjania, L., et al. (2018). Targeting KRAS Mutant Cancers with a Covalent G12C-Specific Inhibitor. Cell *172*, 578–589.e17. https://doi.org/10.1016/j.cell.2018.01.006.

24. Xu, F., He, Q., Li, X., Chang, C.-K., Wu, L.-Y., Zhang, Z., Liu, L., Shi, W.-H., Zhu, Y., Zhao, Y.-S., et al. (2014). Rigosertib as a selective anti-tumor agent can ameliorate multiple dysregulated signaling transduction pathways in high-grade myelodysplastic syndrome. Sci. Rep. *4*, 7310. https://doi.org/10.1038/srep07310.

25. Martinez Molina, D., Jafari, R., Ignatushchenko, M., Seki, T., Larsson, E.A., Dan, C., Sreekumar, L., Cao, Y., and Nordlund, P. (2013). Monitoring Drug Target Engagement in Cells and Tissues Using the Cellular Thermal Shift Assay. Sci. Technol. Humanit. *341*, 84–87. https://doi.org/10.1126/science.1233606.

26. Miettinen, T.P., and Björklund, M. (2014). NQO2 Is a Reactive Oxygen Species Generating Off-Target for Acetaminophen. Mol Pharmaceut *11*, 4395–4404. https://doi.org/10.1021/mp5004866.

27. Yissachar, N., Salem, H., Tennenbaum, T., and Motro, B. (2006). Nek7 kinase is enriched at the centrosome, and is required for proper spindle assembly and mitotic progression. FEBS Lett. *580*, 6489–6495. https://doi.org/10.1016/j.febslet.2006.10.069.

28. Shi, H., Wang, Y., Li, X., Zhan, X., Tang, M., Fina, M., Su, L., Pratt, D., Bu, C.H., Hildebrand, S., et al. (2016). NLRP3 activation and mitosis are mutually exclusive events coordinated by NEK7, a new inflammasome component. Nat. Immunol. *17*, 250–258. https://doi.org/10.1038/ni.3333.

29. Bertran, M.T., Sdelci, S., Regué, L., Avruch, J., Caelles, C., and Roig, J. (2011). Nek9 is a Plk1-activated kinase that controls early centrosome separation through Nek6/7 and Eg5. EMBO J. *30*, 2634–2647. https://doi.org/10.1038/emboj.2011.179.

30. van de Kooij, B., Creixell, P., van Vlimmeren, A., Joughin, B.A., Miller, C.J., Haider, N., Simpson, C.D., Linding, R., Stambolic, V., Turk, B.E., and Yaffe, M.B. (2019). Comprehensive substrate specificity profiling of the human Nek kinome reveals unexpected signaling outputs. eLife *8*, e44635. https://doi.org/10.7554/eLife.44635.

31. Bhattacharyya, B., Panda, D., Gupta, S., and Banerjee, M. (2008). Anti-mitotic activity of colchicine and the structural basis for its interaction with tubulin. Med. Res. Rev. *28*, 155–183. https://doi.org/10.1002/med.20097.

32. Zhou, X., Xiao, Q., Fu, D., Zhang, H., Tang, Y., He, J., Hu, Y., Kong, X., Teng, F., Liu, X., et al. (2021). Efficacy of rigosertib, a small molecular RAS signaling disrupter for the treatment of KRAS -mutant colorectal cancer. Cancer Biol. Med. *19*, 213–228. https://doi.org/10.20892/j.issn.2095-3941.2020.0532.

33. Baker, S.J., Cosenza, S.C., Athuluri-Divakar, S., Reddy, M.V.R., Vasquez-Del Carpio, R., Jain, R., Aggarwal, A.K., and Reddy, E.P. (2020). A Contaminant Impurity, Not Rigosertib, Is a Tubulin Binding Agent. Mol. Cell *79*, 180–190.e4. https://doi.org/10.1016/j.molcel.2020.05.024.

34. Shi, R., Radulovich, N., Ng, C., Liu, N., Notsuda, H., Cabanero, M., Martins-Filho, S.N., Raghavan, V., Li, Q., Mer, A.S., et al. (2020). Organoid Cultures as Preclinical Models of Non–Small Cell Lung Cancer. Clin. Cancer Res. *26*, 1162–1174. https://doi.org/10.1158/1078-0432.ccr-19-1376.

35. Terashima, Y., Matsumoto, M., Iida, H., Takashima, S., Fukuizumi, A., Takeuchi, S., Miyanaga, A., Terasaki, Y., Kasahara, K., and Seike, M. (2023). Predictive Impact of Diffuse Positivity for TTF-1 Expression in Patients Treated With Platinum-Doublet Chemotherapy Plus Immune Checkpoint Inhibitors for Advanced Nonsquamous NSCLC. JTO Clin. Res. Rep. *4*, 100578. https://doi.org/10.1016/j.jtocrr.2023.100578.

36. Rahmani, F., Hashemzehi, M., Avan, A., Barneh, F., Asgharzadeh, F., Moradi Marjaneh, R., Soleimani, A., Parizadeh, M., Ferns, G.A., Ghayour Mobarhan, M., et al. (2021). Rigosertib elicits potent anti-tumor responses in colorectal cancer by inhibiting Ras signaling pathway. Cell. Signal. *85*, 110069. https://doi.org/10.1016/j.cellsig.2021.110069.

37. Man, S.M., and Kanneganti, T.D. (2015). Regulation of inflammasome activation. Immunol. Rev. *265*, 6–21. https://doi.org/10.1111/imr.12296.

38. Bauernfeind, F.G., Horvath, G., Stutz, A., Alnemri, E.S., Macdonald, K., Speert, D., Fernandes-Alnemri, T., Wu, J., Monks, B.G., Fitzgerald, K.A., et al. (2009). Cutting Edge: NF-κB Activating Pattern Recognition and Cytokine Receptors License NLRP3 Inflammasome Activation by Regulating NLRP3 Expression. J. Immunol. *183*, 787–791. https://doi.org/10.4049/jimmunol.0901363.

39. Sharma, B.R., and Kanneganti, T.-D. (2021). NLRP3 inflammasome in cancer and metabolic diseases. Nat. Immunol. *22*, 550–559. https://doi.org/10.1038/s41590-021-00886-5.

40. Zhou, R., Yazdi, A.S., Menu, P., and Tschopp, J. (2011). A role for mitochondria in NLRP3 inflammasome activation. Nature *469*, 221–225. https://doi.org/10.1038/nature09663.

41. He, Y., Zeng, M.Y., Yang, D., Motro, B., and Núñez, G. (2016). Nek7 is an essential mediator of NLRP3 activation downstream of potassium efflux. Nature *530*, 354–357.

42. Shi, J., Zhao, Y., Wang, K., Shi, X., Wang, Y., Huang, H., Zhuang, Y., Cai, T., Wang, F., and Shao, F. (2015). Cleavage of GSDMD by inflammatory caspases determines pyroptotic cell death. Nature *526*, 660–665. https://doi.org/10.1038/nature15514.

43. Franklin, B.S., Bossaller, L., De Nardo, D., Ratter, J.M., Stutz, A., Engels, G., Brenker, C., Nordhoff, M., Mirandola, S.R., Al-Amoudi, A., et al. (2014). The adaptor ASC has extracellular and 'prionoid' activities that propagate inflammation. Nat. Immunol. *15*, 727–737. https://doi.org/10.1038/ni.2913.

44. Martinon, F., Burns, K., and Tschopp, J. (2002). The Inflammasome. Mol. Cell *10*, 417–426. https://doi.org/10.1016/s1097-2765(02)00599-3.

45. Kayagaki, N., Stowe, I.B., Lee, B.L., O'Rourke, K., Anderson, K., Warming, S., Cuellar, T., Haley, B., Roose-Girma, M., Phung, Q.T., et al. (2015). Caspase-11 cleaves gasdermin D for non-canonical inflammasome signalling. Nature *526*, 666–671. https://doi.org/10.1038/nature15541.

46. Chanput, W., Mes, J.J., and Wichers, H.J. (2014). THP-1 cell line: an in vitro cell model for immune modulation approach. Int. Immunopharmacol. *23*, 37–45. https://doi.org/10.1016/j.intimp.2014.08.002.

47. Han, J.H., Tweedell, R.E., and Kanneganti, T.D. (2023). Evaluation of Caspase Activation to Assess Innate Immune Cell Death. J. Vis. Exp. https://doi.org/10.3791/64308.

48. Inaba, K., Masui, S., Iida, H., Vavassori, S., Sitia, R., and Suzuki, M. (2010). Crystal structures of human Ero1α reveal the mechanisms of regulated and targeted oxidation of PDI. EMBO J. *29*, 3330–3343. https://doi.org/10.1038/emboj.2010.222.

49. Groß, C.J., Mishra, R., Schneider, K.S., Médard, G., Wettmarshausen, J., Dittlein, D.C., Shi, H., Gorka, O., Koenig, P.-A., Fromm, S., et al. (2016). K^+ Efflux-Independent NLRP3 Inflammasome Activation by Small Molecules Targeting Mitochondria. Immunity (Camb., Mass.) *45*, 761–773. https://doi.org/10.1016/j.immuni.2016.08.010.

50. Zhang, J., Zhou, Y., Li, N., Liu, W.T., Liang, J.Z., Sun, Y., Zhang, W.X., Fang, R.D., Huang, S.L., Sun, Z.H., et al. (2020). Curcumol Overcomes TRAIL Resistance of Non-Small Cell Lung Cancer by Targeting NRH: Quinone Oxidoreductase 2 (NQO2). Adv. Sci. *7*, 2002306. https://doi.org/10.1002/advs.202002306.

51. Chhour, M., Perio, P., Gayon, R., Ternet-Fontebasso, H., Ferry, G., Nepveu, F., Boutin, J.A., Sudor, J., and Reybier, K. (2021). Association of NQO2 With UDP-Glucuronosyltransferases Reduces Menadione Toxicity in Neuroblastoma Cells. Front. Pharmacol. *12*, 660641. https://doi.org/10.3389/fphar.2021.660641.

52. Bae, Y.S., Oh, H., Rhee, S.G., and Yoo, Y.D. (2011). Regulation of Reactive Oxygen Species Generation in Cell Signaling. Mol. Cells *32*, 491–509. https://doi.org/10.1007/s10059-011-0276-3.

53. Zhang, J., Wang, X., Vikash, V., Ye, Q., Wu, D., Liu, Y., and Dong, W. (2016). ROS and ROS-Mediated Cellular Signaling. Oxid. Med. Cell. Longev. *2016*, 4350965. https://doi.org/10.1155/2016/4350965.

54. Günther, J.K., Nikolajevic, A., Ebner, S., Troppmair, J., and Khalid, S. (2020). Rigosertib-Activated JNK1/2 Eliminate Tumor Cells through p66Shc Activation. Biology (Basel) *9*, 99. https://doi.org/10.3390/biology9050099.

55. Zhang, C.-C., Li, C.-G., Wang, Y.-F., Xu, L.-H., He, X.-H., Zeng, Q.-Z., Zeng, C.-Y., Mai, F.-Y., Hu, B., and Ouyang, D.-Y. (2019). Chemotherapeutic paclitaxel and cisplatin differentially induce pyroptosis in A549 lung cancer cells via caspase-3/GSDME activation. Apoptosis *24*, 312–325. https://doi.org/10.1007/s10495-019-01515-1.

56. Wang, Y., Gao, W., Shi, X., Ding, J., Liu, W., He, H., Wang, K., and Shao, F. (2017). Chemotherapy drugs induce pyroptosis through caspase-3 cleavage of a gasdermin. Nature *547*, 99–103. https://doi.org/10.1038/nature22393.

57. Yan, H., Luo, B., Wu, X., Guan, F., Yu, X., Zhao, L., Ke, X., Wu, J., and Yuan, J. (2021). Cisplatin Induces Pyroptosis via Activation of MEG3/NLRP3/caspase-1/GSDMD Pathway in Triple-Negative Breast Cancer. Int. J. Biol. Sci. *17*, 2606–2621. https://doi.org/10.7150/ijbs.60292.

58. Zhang, Y., Yang, H., Sun, M., He, T., Liu, Y., Yang, X., Shi, X., and Liu, X. (2020). Alpinumisoflavone suppresses hepatocellular carcinoma cell growth and metastasis via NLRP3 inflammasome-mediated pyroptosis. Pharmacol. Rep. *72*, 1370–1382. https://doi.org/10.1007/s43440-020-00064-8.

59. Wang, Y., Yin, B., Li, D., Wang, G., Han, X., and Sun, X. (2018). GSDME mediates caspase-3-dependent pyroptosis in gastric cancer. Biochem Bioph Res Co *495*, 1418–1425. https://doi.org/10.1016/j.bbrc.2017.11.156.

60. Teng, J.-F., Mei, Q.-B., Zhou, X.-G., Tang, Y., Xiong, R., Qiu, W.-Q., Pan, R., Law, B.Y.-K., Wong, V.K.-W., Yu, C.-L., et al. (2020). Polyphyllin VI Induces Caspase-1-Mediated Pyroptosis via the Induction of ROS/NF-κB/NLRP3/GSDMD Signal Axis in Non-Small Cell Lung Cancer. Cancers *12*, 193. https://doi.org/10.3390/cancers12010193.

61. Liu, J., Zhang, X., Cheng, Y., and Cao, X. (2021). Dendritic cell migration in inflammation and immunity. Cell. Mol. Immunol. *18*, 2461–2471. https://doi.org/10.1038/s41423-021-00726-4.

62. Ma, Y., Adjemian, S., Mattarollo, S.R., Yamazaki, T., Aymeric, L., Yang, H., Portela Catani, J.P., Hannani, D., Duret, H., Steegh, K., et al. (2013). Anticancer Chemotherapy-Induced Intratumoral Recruitment and Differentiation of Antigen-Presenting Cells. Immunity *38*, 729–741. https://doi.org/10.1016/j.immuni.2013.03.003.

63. Wang, L., Geng, H., Liu, Y., Liu, L., Chen, Y., Wu, F., Liu, Z., Ling, S., Wang, Y., and Zhou, L. (2023). Hot and cold tumors: Immunological features and the therapeutic strategies. MedComm *4*, e343. https://doi.org/10.1002/mco2.343.

64. Schneider, C.A., Rasband, W.S., and Eliceiri, K.W. (2012). NIH Image to ImageJ: 25 years of image analysis. Nat. Methods *9*, 671–675. https://doi.org/10.1038/nmeth.2089.

65. Lee, P.-H., Huang, X.X., Teh, B.T., and Ng, L.-M. (2019). TSA-CRAFT: A Free Software for Automatic and Robust Thermal Shift Assay Data Analysis. SLAS Discov. *24*, 606–612. https://doi.org/10.1177/2472555218823547.

66. Farin, H.F., Van Es, J.H., and Clevers, H. (2012). Redundant Sources of Wnt Regulate Intestinal Stem Cells and Promote Formation of Paneth Cells. Gastroenterology (New York, N. Y., 1943) *143*, 1518–1529.e7. https://doi.org/10.1053/j.gastro.2012.08.031.

67. Wallaschek, N., Niklas, C., Pompaiah, M., Wiegering, A., Germer, C.T., Kircher, S., Brändlein, S., Maurus, K., Rosenwald, A., Yan, H.H.N., et al. (2019). Establishing Pure Cancer Organoid Cultures: Identification, Selection and Verification of Cancer Phenotypes and Genotypes. J. Mol. Biol. *431*, 2884–2893. https://doi.org/10.1016/j.jmb.2019.05.031.

68. van Ineveld, R.L., Ariese, H.C.R., Wehrens, E.J., Dekkers, J.F., and Rios, A.C. (2020). Single-Cell Resolution Three-Dimensional Imaging of Intact Organoids. J. Vis. Exp. https://doi.org/10.3791/60709.

69. Forster, B., Van De Ville, D., Berent, J., Sage, D., and Unser, M. Extended Depth-Of-Focus for Multi-Channel Microscopy Images: A Complex Wavelet Approach. (IEEE), pp. 660-663.

70. Ritchie, M.E., Phipson, B., Wu, D., Hu, Y., Law, C.W., Shi, W., and Smyth, G.K. (2015). limma powers differential expression analyses for RNA-sequencing and microarray studies. Nucleic Acids Res. *43*, e47. https://doi.org/10.1093/nar/gkv007.

STAR★METHODS

KEY RESOURCES TABLE

REAGENT or RESOURCE	SOURCE	IDENTIFIER
Antibodies		
CRAF	Cell Signaling Technology	#9422; RRID: AB_390808
pCRAF Ser338	Cell Signaling Technology	#9427; RRID: AB_2067317
MEK1/2	Cell Signaling Technology	#2352; RRID: AB_10693788
pMEK1/2 Ser217/221	Cell Signaling Technology	#9154; RRID: AB_2138017
ERK1/2	Cell Signaling Technology	#9102; RRID: AB_330744
pERK1/2 Thr202/204	Cell Signaling Technology	#9101; RRID: AB_331646
pSAPK/JNK Thr183/185	Cell Signaling Technology	#4668; RRID: AB_823588
SAPK/JNK	Cell Signaling Technology	#9252; RRID: AB_2250373
Caspase-3	Cell Signaling Technology	#9662; RRID: AB_331439
Pan-RAS	Santa Cruz	sc-166691; RRID: AB_2154229
Anti-GST	Santa Cruz	sc-138; RRID: AB_627677
SOS1	Santa Cruz	sc-17793; RRID: AB_628269
pCRAF Ser642	Sigma-Aldrich	SAB4301383; RRID: AB_2554319
Vinculin	Sigma-Aldrich	SAB4200080; RRID: AB_10604160
HRP conjugated β-Actin	Abcam	ab49900; RRID: AB_867494
GSDMD	Abcam	ab210070; RRID: AB_2893325
ERO1L	Abcam	ab177156; RRID: AB_2941804
NQO2	Abcam	ab236917
Cyclin D1	Abcam	1677-1; RRID: AB_562097
HRP conjugated mouse IgG	Thermo Fisher Scientific	A16066; RRID: AB_2534739
HRP conjugated rabbit IgG	Thermo Fisher Scientific	A16096; RRID: AB_2534770
Cytokeratin 7	Thermo Fisher Scientific	#MA5-32173; RRID: AB_2809461
Acetylated Tubulin	Sigma-Aldrich	#T7451; RRID:AB_609894
rabbit AlexaFluor 488	Invitrogen	#A-11008; RRID: AB_14365
α-mouse AlexaFluor 647	Invitrogen	#A-21235; RRID: AB_2535804
Biological samples		
Normal human lung organoids	University Medical Center of the JGU Mainz	N/A
3dGRO LUAD – LPTO.54	Sigma-Aldrich	#SCC600
3dGRO LUAD – LPTO.85	Sigma-Aldrich	#SCC601
3dGRO LUAD – XDO.344	Sigma-Aldrich	#SCC603
Chemicals, peptides, and recombinant proteins		
Recombinant Human NQO2 protein	Abcam	ab93933
purified GST-CRAF RBD fusion protein	Thermo Fisher Scientific	#1862334
PMA	Sigma	P1585
LPS	Sigma	L6143
EGF	Corning	354052
Rigosertib	Onconova Inc.	N/A
ON02180.Na	Onconova Inc.	N/A
ON013101	Onconova Inc.	N/A
Rocaglamide	Active biochem	N/A
ARS-1620	Selleckchem	S8707
NAC	Sigma	A9165
Colchicine	Sigma	C9754
SP600125	Selleckchem	S1460

(*Continued on next page*)

Continued

REAGENT or RESOURCE	SOURCE	IDENTIFIER
Polybrene	Santa Cruz	#sc-134220
Puromycin	Carl Roth	#0240.3
Lipofectamine RNAiMAX Transfection Reagent	Thermo Fisher Scientific	13778030
CellROX Green Reagent	Thermo Fisher Scientific	C10444
NMEH	Cayman chemical	23226
FAD	Selleckchem	E0705
Menadione	Sigma	M-5625
Collagenase II	Worthington Biochemical corporation	#LS004174
Hyaluronidase	Sigma	#H4272
Primocin	InvivoGen	#ant-pm-1
Nicotinamide	Sigma-Aldrich	#N0636
A83-01 (TGF-βi)	Tocris Bioscience	#2939
SB 202190 (p38i)	Tocris Bioscience	#1264
FGF7	Peprotech	#100-19
FGF10	Peprotech	#100-26
FGF4	Peprotech	#100-31
CHIR 99021	Miliporesigma	#SML1046
SAG	Enzo	#ALX-270-426-M001
Rho kinase inhibitor Y-27632	Abmole	#M1817
Critical commercial assays		
Caspase-Glo® 1 Inflammasome Assay	Promega	G9952
Human IL-1 beta Uncoated ELISA	Invitrogen	#88-7261
Human IL-18 ELISA Kit	Invitrogen	#BMS267-2
Tubulin Polymerization Assay Kit	Cytoskeleton	BK006P
CellTiter-Glo® 3D Cell Viability Assay	Promega	#G9682
Deposited data		
CETSA-MS	Pelagobio	Zenodo: https://doi.org/10.5281/zenodo.15393885
Original western blot images	N/A	Zenodo: https://doi.org/10.5281/zenodo.15393972
Experimental models: Cell lines		
HeLa	DSMZ	N/A
HEK-293T	gift from Ulf Rapp, University of Wurzburg, Germany	N/A
BHK-21	ATCC	CCL-10
H358	ATCC	CRL-5807
THP1 monocytes	Chanput et al.[46]	N/A
BMDMs	Dr. Kanneganti (Department of Immunology, St. Jude Children's Research Hospital)[47]	N/A
Oligonucleotides		
Negative control siRNA (siCo)	Qiagen	#1027310
siERO1L	Qiagen	#SI03135384
siNQO2	Qiagen	#SI00661290
non-targeting control shRNA (shCo)	MISSION pLKO.1 puro (Sigma)	# SHC001
shERO1L	MISSION shRNA Human Library (Sigma)	TRCN0000059754, NM_014584.1-752s1c1
shNQO2	MISSION shRNA Human Library (Sigma)	TRCN0000304012, NM_000904.3-849s21c1

(*Continued on next page*)

Continued

REAGENT or RESOURCE	SOURCE	IDENTIFIER
Software and algorithms		
Prism 10.3.0 (507)	GraphPad	https://www.graphpad.com/updates/prism-10-3-0-release-notes; RRID: SCR_002798
ImageJ 1.53c	Schneider et al.[64]	https://imagej.net
Image Lab 6.0.1.	Bio-Rad	https://www.bio-rad.com/it-it/product/image-lab-software?ID=KRE6P5E8Z
Imaris version 9.3.1	Oxford Instruments	https://imaris.oxinst.com/support/imaris-release-notes/
Proteome Discoverer 2.4 software	Thermo Fisher Scientific	N/A
TSA-CRAFT software	Lee PH et al.[65]	https://bioserv.cbs.cnrs.fr/TSA_CRAFT/

EXPERIMENTAL MODEL AND STUDY PARTICIPANT DETAILS

Cell lines

HeLa cells and HEK-293T cells were cultured in DMEM supplemented with 10% heat-inactivated fetal bovine serum (FBS) (Sigma, F9665). BHK-21 cells were cultured in EMEM supplemented with 1x non-essential amino acid (GIBCO, M7145) and 10% FBS. H358 (KRAS G12C) cells were cultured in RPMI 1640 supplemented with 10% heat-inactivated fetal bovine serum (FBS) and stimulated, if needed, with 100 ng/mL human epidermal growth factor (EGF) (Cat# RP-10927, Invitrogen) for 5 min. THP1 monocytes cells were cultured in RPMI 1640 supplemented with 10% heat-inactivated fetal bovine serum (FBS) and differentiated into macrophages with 300 ng/mL phorbol 12-myristate 13-acetate (PMA) (Sigma, P1585) overnight. Then THP1 monocytes and macrophages were stimulated with lipopolysaccharide (LPS) (Sigma, L6143) for 30 min and 6 h of 2 μM rigosertib treatment.

Sex of the cell lines.

- HeLa: Female
- HEK-293T: Female
- BHK-21 (ATCC CCL-10): Male
- H358 (ATCC CRL-5807): Male
- THP1 monocytes: Male + Female

Human tissue material

Normal human lung organoids were derived from tumor adjacent normal lung after tumor resection. Tissue samples used in this study were provided by the University Medical Center of the JGU Mainz. Written informed consent was obtained from all patients, and the study was approved by the ethical committee at the University Medical Center of the JGU Mainz.

Lung cancer organoids were purchased form Sigma and maintained according to the manufacturers instructions.

Sex of the used organoids:

- LPTO54 (#SCC600): Male
- LPTO85 (#SCC601): Female
- PDXO344 (#SCC603): Male
- P2N and P4N: unknown

Bone marrow derived macrophages (BMDMs)

Primary BMDMs (*WT*, *Nlrp3*-/- and *Asc*-/-) were kindly provided by Dr. Kanneganti (Department of Immunology, St. Jude Children's Research Hospital). The cells were cultured and employed to assess caspase-1 activity as described in.[47] Briefly, a culture medium was prepared with 290 mL IMDM (GIBCO, 12440-053) supplemented with 10% FBS, 150 mL L929-conditioned medium (Cellbiologics, 3368), 5 mL (1%) non-essential amino acids (Sigma, M7145), and 5 mL (1%) penicillin and streptomycin (Thermo Fisher Scientific, 15070-063). Frozen cells were resuspended in 20 mL BMDM culture media. 70 μm cell strainer was used to filter the BMDM culture media containing the cells. The resulting cell suspension was plated, which contains the bone marrow progenitor cells, into two 150 mm tissue culture dishes by adding 10 mL to each. Then, an additional 10 mL of BMDM culture media was added to each dish. The plated bone marrow progenitor cells were incubated at 37°C for 3 days. Then, each dish was removed, and an additional 8 mL of BMDM culture media was added and returned to the incubator at 37°C. On day 5 after the initial plating, each dish was removed, and an additional 5 mL of BMDM culture media was added and returned to the incubator at 37°C. On day 6, the media from each dish was discarded and cells were gently scraped to perform the experiment. BMDMs were then seeded into 12-well

plates with antibiotic-free medium at a density of 1×10^6 cells per well and incubated overnight. Next day, the culture media was replaced with stimulation media (DMEM supplemented with 10% heat-inactivated FBS and antibiotics) and cells were treated with rigosertib 2 μM for 18 h. The supernatant was harvested for caspase-1 detection by Caspase-Glo® 1 Inflammasome Assay.

METHOD DETAILS

Thermal shift assay

Thermal Shift Assay reactions were prepared in triplicates in a MicroAmp Fast Optical 96-Well Reaction Plate (Applied Biosystems #4346907) using Protein Thermal Shift Dye Kit (Applied Biosystems #4461146). Each reaction well contained 1 μg of purified GST-C-RAF RBD fusion protein (Thermo Fisher Scientific #1862334) or purified GST, 1 μL DMSO or 1 μL of 2 mM rigosertib stock in DMSO, and Protein Thermal Shift Dye in 1x buffer, for a final reaction volume of 20 μL per well. Melt Curve experiment was performed with StepOne Real-Time PCR system (Applied Biosystems) and data was analyzed with TSA-CRAFT software.[65]

Competition assay for binding to C-RAF-RBD

Purified GST-C-RAF-RBD (2.5 μg per binding reaction) immobilized on beads was incubated at 4°C overnight with either DMSO or rigosertib (diluted in DMSO) at a final concentration of 2, 10 or 50 μM. HeLa cells were serum-starved for 18 h, and stimulated with EGF at 50 ng/mL for 5 min before preparation of cell lysates in RAS binding buffer (25 mM Tris-HCl pH 7.2, 150 mM NaCl, 5 mM $MgCl_2$, 1% NP-40, 5% glycerol with protease inhibitor cocktail). For each condition, 200 μL of cell lysate were incubated with the binding reaction for 1h at 4°C.

For *in vitro* competition assay, 2.5 μg of immobilized GST-C-RAF-RBD per condition was incubated overnight at 4°C in 200 μL of RAS binding buffer containing DMSO, or 2, 10, or 50 μM of either rigosertib or ON01280.Na control compound. To prepare *in vitro* GDP- or GTPγS-loaded RAS, 0.1 μg of purified $KRAS^{wt}$ was added to 100 μL RAS binding buffer with 2 μL of 0.5M EDTA, and incubated with 1 μL of 100 mM GDP or 10 mM GTPγS for 15 min on a ThermoMixer at 30°C. The loading reaction was terminated by placing the tube on ice and adding 6.4 μL of 1 M $MgCl_2$. These loading reactions were then incubated for 1 h at 4°C with 200 μL of C-RAF-RBD binding reaction for each condition.

After incubation, the beads were washed twice with RAS binding buffer to remove unbound proteins, and resuspended in 50 μL of SDS-PAGE sample buffer (125 mM Tris-HCl pH 6.8, 4% SDS, 10% glycerol, bromophenol blue, 0.1 M DTT). The levels of active RAS bound to C-RAF-RBD were then analyzed by Western blot.

NanoBiT assay

The NanoBiT constructs were generated using N-terminal LgBit and C-terminal SmBit plasmids from Promega as described in our previous study.[20]

For in cell NanoBiT, BHK-21 cells were transfected with SmBiT-C-RAF-RBD and either LgBiT-KRAS G12C, LgBiT-KRAS G12V, LgBiT-NRAS G12V or LgBiT-HRAS G12V using PEI transfection reagent (Polyethylenimine, PEI 25000, Sigma). Cells were harvested 24 h after transfection, and seeded in a white 96-well plate. After an additional day, the medium was changed to serum free medium and treated for 2 to 8 h with rigosertib, ON02180.Na, rocaglamide (Active biochem), or ARS-1620 (Selleckchem, S8707).

For cell-free NanoBiT system, HEK-293T cells were transfected with SmBiT-C-RAF-RBD and either LgBiT-KRAS G12C or G12V. Total cell lysates were prepared 48 h after transfection in 1 mL of Passive Lysis Buffer (Promega). Cell lysates were dispensed in white 96-well plate (40 μg, 100 μL/well) with increasing concentration of rigosertib, ON02180.Na or ARS-1620, and incubated on ice for 2 to 4 h.

After treatment, Nano-Glo Live Cell Substrate (Promega N205A) was added to each well according to the manufacturer's instructions. Luminescence was measured using a TECAN Spark microplate reader with an integration time of 1,000 ms.

Active RAS pulldown

HeLa cells were cultured in 6-well plates in complete DMEM. Once the cells reach near confluence (70–80%), medium was exchanged to serum-free medium for 24 h before cell collection, and treated during the indicated time with rigosertib at 2 μM, colchicine at 100 nM (Sigma, C9754) and JNK inhibitor SP600125 at 10 μM (Selleckchem, S1460). After treatment, cells were stimulated with EGF at 100 ng/mL for 5 min. Total cell lysates were prepared in 400 μL of RAS binding buffer. Protein concentration was determined using Pierce 660 nm Protein Assay Reagent (Thermo Scientific), and then adjusted to obtain equal protein concentration for all the samples. Before active RAS pulldown, 20% of the total cell lysates was kept for Western blot analysis. C-RAF-RBD immobilized on agarose beads (20 μL) was added to the rest of lysate and rotated at 4°C for 1 h. After incubation, the beads were washed twice with RAS binding buffer, and resuspended in 50 μL of SDS-PAGE sample buffer for Western blot analysis.

SDS-PAGE and western blotting

After a denaturation step of 5 min at 95°C, proteins were separated on 12%, 10% or 7.5% SDS-PAGE gels and transferred to nitrocellulose membrane for immunoblotting analysis. The membranes were blocked with 3% BSA/TBST (20 mM Tris-HCl, pH 7.5, 150 mM NaCl, 0.05% Tween 20) for one hour at room temperature, then incubated overnight at 4°C with primary antibody diluted at 1/1,000 in 1% BSA/TBST. The membranes were then washed with TBST and incubated with HRP-conjugated secondary antibody diluted 1/40,000 in TBST for one hour at room temperature. After washes in TBST, the signal was visualized using Immobilon Western

Chemiluminescent HRP Substrate (Millipore) and ChemiDoc Touch Imaging System (Bio-Rad). Quantification of immunoblots was performed with ImageJ 1.53c or Image Lab 6.0.1.

Antibodies

Antibodies directed against C-RAF (#9422), p-c-RAF Ser338 (#9427), MEK1 (#2352), pMEK1/2 Ser217/221 (#9154), ERK1/2 (#9102), pERK1/2 Thr202/Tyr204 (#9101), p-SAPK/JNK (Thr183/Tyr185) (#4668), SAPK/JNK (#9252) and Caspase-3 (#9662) were purchased from Cell Signaling Technology. Anti-pan RAS (sc-166691), anti-GST (sc-138) and anti-SOS1 (sc-17793) antibodies were purchased from Santa Cruz. Antibodies directed against p-C-RAF Ser642 (SAB4301383) and Vinculin (SAB4200080) were obtained from Sigma. HRP conjugated β-Actin antibody (ab49900), anti-human GSDMD (ab210070), ERO1L (ab177156) and NQO2 (ab236917) were purchased from Abcam and anti-Cyclin D1 antibody (1677-1) from Abcam. Horseradish peroxidase-conjugated antibodies for Mouse and Rabbit IgG were obtained from Thermo Fisher Scientific (A16066 and A16096, respectively).

In vitro tubulin polymerization

In vitro tubulin polymerization assay was performed according to the manufacturer's instruction (Tubulin Polymerization Assay Kit, Cytoskeleton, BK006P). The assay was performed with inhibitors indicated in the figure legend and the value was obtained by using TECAN Spark micro plate reader.

NQO2 enzymatic activity assay

The enzymatic activity of the recombinant human NQO2 protein was determined spectrophotometrically at 25°C. 100 ng of recombinant NQO2 protein was mixed with 50 μL of 50 mM Tris-KOH buffer, pH 7.4, with 1 μM FAD, 0.01% Tween 20 and 0.18 mg/mL BSA. Varying concentrations of rigosertib were used into the reaction mix. Imatinib is known that inhibits the NQO2 activity and it was used as a positive control. Enzymatic reactions were initiated by adding 300 μM menadione as a substrate along with 500 μM 1-Methyl-1,4-dihydronicotinamide (NMEH) as a cosubstrate. 600 μM MTT was added at the end and the absorbance of the samples was measured at 595 nm.

Thermal shift assay

4×10^6 H358 cells were treated with either dmso or rigosertib 20 μM for 6 h. Then, lysates were collected and gradient heating (30, 31.7, 34.8, 39.3, 45.3, 49.9, 53°C and 55°C) was performed by using qPCR. Western blotting was used to detect the differences in the denaturation of ERO1A and NQO2 proteins after treatment with rigosertib.

Lentiviral-mediated knockdown of CETSA MS revealed targets

All shRNAs plasmids were purified from the MISSION shRNA Human Library (Sigma) following manufacturer's instructions. As control the non-targeting control shRNA (shCo) MISSION pLKO.1 puro (Cat# SHC001) was included.

shRNA targeting ERO1L (ERO1A), NQO2 and NEK7
shERO1L TRCN0000059754, NM_014584.1-752s1c1,
CCGGGCTGAATATGTAGATTTGCTTCTCGAGAAGCAAATCTACATATTCAGCTTTTTG
shNQO2 TRCN0000304012, NM_000904.3-849s21c1,
CCGGCCACTCCAGCATGGCACATTACTCGAGTAATGTGCCATGCTGGAGTGGTTTTTG.

For the production of lentiviral particles, the following packaging plasmids were used: pHDM-G (encoding VSV-G), pHDM Hgpm2 (encoding codon-optimized HIV gag-pol proteins), pHDM tat 1b (encoding HIV Tat1b protein) and pRC CMV-Rev1b (encoding HIV rev protein). Lentiviral particles were generated following standard protocols. In short, lentiviral supernatants were produced in 293T cells by co-transfection of the cells with lentiviral packaging plasmids (0.3 μg each), lentiviral expression constructs (1 μg) and 10.8 μL of 10 mM polyethylenimine (PEI). The viral particles were harvested after 48 h and sterile-filtered. H358 cells were infected with lentiviral particles in the presence of 10 μg/mL of polybrene (Cat# sc-134220, Santa Cruz). Cells were then selected with puromycin 2.5 μg/mL (Cat# 0240.3, Carl Roth), until a stable knockdown was achieved.

siRNA transfection

siRNAs were purchased from Qiagen.

siERO1L FlexiTube siRNA 5 nmol, siRNA Name: Hs_ERO1L_5, Cat# SI03135384.
Sense strand: 5′-AAGTGACTACTTTAGGTATTA-3′
siNQO2 FlexiTube siRNA 5 nmol, siRNA Name: Hs_NQO2_2, Cat# SI00661290.
Sense strand: 5′-CCGCATGTGTCTGTATTCATA-3′
Negative control siRNA (siCo) Cat# 1027310

2×10^5 cells/well in 12-well plates were transfected with the transfusing Lipofectamine RNAiMAX Transfection Reagent (Thermo Fisher Scientific, 13778030) by spinoculation according to the manufacturer's instructions. For the spinoculation transfection, cells were centrifuged at 800 x *g* for 30 min at 32°C with the transfection reagents. Medium was exchanged 24 h post-transfection for medium without FBS and cells were treated with rigosertib 2 μM. Depending on the type of the experiment, 3 or 24 h after treatment, lysates were harvested for protein extraction. In addition, the knockdown was verified by Western blot.

Transient transfections of stably transfected cells

H358 cells stably transfected with shRNA targeting ERO1L (ERO1A), NQO2 or with control empty vector shRNA (shCo) were transiently transfected with either a negative control siRNA (siCo), siERO1L or siNQO2 in the presence of transfusing Lipofectamine RNAiMAX Transfection Reagent. After overnight transfection, medium was exchanged to serum-free medium with rigosertib 2 μM for 3 or 24 h. Cells were analyzed by western blot.

Enzyme-linked immunosorbent assay (ELISA)

Secreted protein concentration of IL-18 and IL-1β were measured by ELISA. The assays were performed according to manufacturer's instructions (Human IL-18 ELISA Kit, Cat# BMS267-2, Human IL-1 beta Uncoated ELISA, Cat# 88-7261, and Mouse IL-1 bets ELISA Kit, Cat# BMS6002, Invitrogen).

Caspase-1 activity

The caspase-1 activity was measured using the Caspase-Glo® 1 Inflammasome Assay (Promega, G9952). The assay was performed according to manufacturer's instructions.

Live-cell imaging and cell tracking analyses

ERO1A and NQO2 knockdown H358 cells were cultured in sterile chambers (1×10^4 cells/well) (μ-slide 8-well, ibidi) and treated with rigosertib 2 μM along with CellROX Green Reagent (Thermofisher, C10444) at a final concentration of 5 μM. The chamber with the treated cells was kept under 5% CO_2, 37°C, and 90% humidity in a OkoLabs environmental incubator (H-301K environmental chamber, Oko Touch, Oko Pump, T-Control, and CO_2 control, OkoLabs) on the Leica Confocal microscope table, and the green fluorescence due to ROS generation was detected.

The images of the live cells were acquired with a Leica SP8 confocal microscope using a 10 ×0.3 NA objective, with 488 nm excitation and emission window of 500 nm–560 nm for ROS detection and with simultaneous scanning differential interference contrast transmission imaging in a 1178 μm × 1178 μm frame format with 400 lines per second, 1.15 μm/pixel (1024 × 1024 pixel per frame), and with two times averaging per line with a frame acquisition of every 15 min per selected position within the chamber. The images were first acquired in multiple regions of each cell type for greater than 3 h.

The image sequences were imported into Imaris version 9.3.1 and detected automatically by fluorescence with both the whole-cell spot and whole-cell surface analysis. Then the image sequences processing was done using ImageJ/Fiji. The fluorescence was then selected and reported for all cells within the whole picture frame from each time point (every 15 min for 3 h), and the average fluorescence was measured and comparatively reported from each frame from the start to the end point. The same procedure was followed for all the 3 independent experiments. The graphs were created with GraphPad Prism (RRID:SCR_002798), and significance was determined using two-way ANOVA test.

Organoid derivation from lung tissue

Fresh tissue was cut into small pieces, transferred into conical tubes and incubated for 60 min at 37°C with 18.75 Units Collagenase II (Worthington Biochemical corporation #LS004174), 200 μg Hyaluronidase (Sigma-Aldrich #H4272) and 500 μg Primocin (InvivoGen #ant-pm-1) in 10 mL basal medium (advanced Dulbecco's modified Eagle medium (DMEM)/F12 medium supplemented with 10 mM HEPES and 1x GlutaMAX) on a shaker. Pieces were resuspended vigorously and FCS was added to neutralize the digestion solution. Tubes were spin down and the pellet washed with basal medium (400 x g at 4°C). If necessary, the pellet was treated with TrypLE Express (Gibco #12605010) for 5 to 15 min at 37°C and wash with basal medium. The cell suspension was filtered through a 70 μM cell strainer and after one more washing resuspended in Matrigel for organoid derivation.

Culture of lung normal and 3dGRO LUAD human organoids

Lung organoids and 3dGRO LUAD organoids (Sigma-Aldrich #SCC600, #SCC601 and #SCC603) were embedded in Matrigel (Corning #356255) and four 10μL drops of embedded organoids were pipetted to each well of a 24 well plate (40 μL/well). For polymerization, plates were incubated upside down for 45–60 min at 37°C. Matrigel domes containing lung or 3dGRO LUAD organoids were overlaid with 500 μL of lung organoid or 3dGRO lung organoid media, respectively. Lung organoid media: Basal medium supplemented with 1x B27 supplement (Thermo Fisher Scientific #12587–010), 50 μg/mL Primocin (InvivoGen #ant-pm-1), conditioned medium produced in-house: 20% R-spondin1 (RSP1) conditioned medium, 10% mNoggin conditioned medium, 1.25 mM N-acetyl-L-cysteine (Sigma-Aldrich #A9165), 5 mM Nicotinamide (Sigma-Aldrich #N0636), 500 nM A83-01 (TGF-βi) (Tocris Bioscience #2939), 500 nM SB 202190 (p38i) (Tocris Bioscience #1264), 25 ng/mL FGF7 (Peprotech #100-19) and 100 ng/mL FGF10 (Peprotech #100-26). 3dGRO lung organoid media: Basal medium supplemented with 1x B27 supplement (Thermo Fisher Scientific #12587–010), 50 μg/mL Primocin (InvivoGen #ant-pm-1), conditioned medium produced in-house: 10% mNoggin conditioned medium, 1.25 mM N-acetyl-L-cysteine (Sigma-Aldrich #A9165), 500 nM A83-01 (TGF-βi) (Tocris Bioscience #2939), 25 ng/mL FGF7 (Peprotech #100-19) 100 ng/mL FGF4 (Peprotech #100-31), 250 nM CHIR 99021 (Miliporesigma #SML1046) and 100 nM SAG (Enzo #ALX-270-426-M001). 10 μM Rho kinase inhibitor Y-27632 (Abmole #M1817) was included for the first 2 days after first seeding or splitting.

For passaging, Matrigel domes were incubated with cell recovery solution (Corning #354253) for 45-60min at 4°C and if necessary, pellets were treated with TrypLE Express for 3–5 min at 37°C. Medium was refreshed every 2–3 days.

RSP1 and mNoggin (kind gift from Henner F Farin, Institute for Tumor Biology and Experimental Therapy, Frankfurt) conditioned medium was produced according to the methods described in Farin et al. and Wallaschek et al.[66,67]

Immunofluorescence staining, clearing and image acquisition of organoids

Organoids were stained as previously described by van Ineveld et al.[68] In brief, organoid media was removed and the Matrigel domes were washed once with ice-old PBS. Cell recovery solution was added and the plate was incubated on a shaker for 60 min at 4°C. Released organoids were then transferred to a 15 mL conical tube previously coated with Anti-Adherence Rinsing Solution (Stemcell #07010) and washed with ice-cold PBS (700 x g for 10 min at 4°C). Pellets were resuspended with ice-cold 4% PFA and incubated for 45 min at 4°C. After incubation, 10 mL of PBS with Tween 20 were added and tubes were spin down at 4°C. Organoids were then block with ice-cold organoid washing buffer (OWB) for at least 15 min at 4°C and subsequently transferred to a 48-well plate. Organoids were stained with primary antibodies (Cytokeratin 7 [1:300], Thermofisher #MA5-32173, Acetylated Tubulin [1:300], Sigma #T7451) in OWB overnight on a shaker at 4°C. Stained organoids were washed three times with OWB with mild shaking and incubated overnight with secondary antibodies (α-rabbit AlexaFlour 488 [1:500], Invitrogen #A-11008, α-mouse AlexaFlour 647 [1:1,000], Invitrogen #A-21235) and DAPI (0.5 mg/mL) at 4°C on a shaker. Organoids were washed three times with OWB with mild shaking, transferred to 1.5 mL Eppendorf tubes and spin down. Pellets were resuspended in around 60 μL FUnGI, incubated for 20 min at RT and transferred to slides with coverslips. Samples were analyzed with confocal microscopy using Leica SP-8 microscope (20x, oil immersion) and image processing was done using ImageJ/Fiji.

Cell viability assay Glo 3D

Organoid cell viability was determined using CellTiter-Glo 3D Cell Viability Assay (Promega #G9682) following the manufacters intructions. In brief, organoids were realeased from Matrigel using Cell recovery solution and washed with ice-cold PBS. Pellets were resuspended in 100 μL PBS and transferred to an opaque 96-well plate. Both the plate and the Glo3D solution were incubated at RT for 30 min and 100 μL of Glo3D solution was added to each well. The plate then placed on a shaker (800 rpm) for 5 min and incubated in the dark for 25 min. Luminescence acquisition was done on a TECAN reader.

Live cell imaging of organoids

Organoids were imaged every 24 h using an inverted widefield microscope (Leica DMi8 S TIRF) equipped with an incubation housing system for temperature and CO_2 controlling. Brightfield images were taken with a 5x objective, analyzed using ImageJ/Fiji and are shown after Extended Depth of Field processing.[69]

CETSA

Sample matrix HL60, H358 and K562 cells were cultured in at 37°C, 5% CO_2 in medium with supplements according to standard protocols. For the experiment, the cells were pelleted, washed with Hank's Balanced Salt solution (HBSS, Thermo Fisher Scientific), and pelleted again. Cell viability was measured with trypan blue exclusion and cells with a viability above 90% were used. For the experiment, cell pellets were re-suspended in CETSA buffer (20 mM HEPES, 138 mM NaCl, 5 mM KCl, 2 mM CaCl2, 1 mM MgCl2, pH 7.4) and used as the 2x cell suspension.

For the lysate experiment, cells were lysed by three rounds of freeze-thawing. The lysate was clarified by centrifugation at 30,000 x g for 20 min and used immediately in the CETSA experiment constituting the 2x lysate. For the experiment on intact cells, the cells were incubated with compound at 2 or 20 μM final concentration for 60 min at 37°C. For the lysate experiment, cells were subjected to three freeze/thaw cycles with liquid nitrogen followed by centrifugation at 30,000 x g for 20 min. The supernatant was used as the 2x matrix for the profiling in clarified lysate. The lysate was then incubated with the compound at 2 or 20 μM final concentration for 15 min at room temperature.

Compounds

Rigosertib (RGS) was provided by Onconova Therapeutics as dry powder and stored at −20°C. Colchicine was procured as dry powder from Cayman Chemical. For the experiment RGS was dissolved in water, while Colchicine in DMSO as 10 mM stock solution.

Compressed CETSA MS experiment

For each experiment, the cell suspension or cell lysate was divided into four aliquots each and mixed with an equal volume of either of the two compound concentrations or positive control at 2x final concentration in the experimental buffer. The resulting final concentrations of the compound was 2 and 20 μM; 30 μM for the positive control, 1% DMSO was used as a negative (vehicle) control. Incubations were performed as described above.

Each of the treated cell lysates or cell suspensions were divided into nx12 (12 temperature points, n number of replicates, $n = 5$ for compound-treated and vehicle, $n = 1$ for positive control) that were all subjected to a heat challenge. After heating, the cell suspensions were subjected to 3 freeze/thaw cycles. All temperature points for each test condition were pooled to generate individual (compressed) samples.

Precipitated proteins were pelleted by centrifugation and supernatants constituting the soluble protein fraction were kept for further analysis.

Protein digestion and labeling

Equal amounts of total protein from each soluble fraction were subjected to reduction, denaturation and alkylation with 2-chloroacetamide. Proteins were subsequently digested with Lys-C and trypsin.

After complete digestion had been confirmed by nano LC-MS/MS, samples were labeled with 16-plex Tandem Mass Tag reagents (TMTPro, Thermo Scientific) according to the manufacturer's protocol.

LC-MS/MS analysis

For each TMT16-plex set, peptides were separated by multidimensional chromatography, and highresolution MS/MS data was acquired with Q Exactive HFx (Thermo Scientific).

Protein identification

Protein identification was performed by database search against 95,607 human protein sequences in Uniprot (UP000005640, download date: 2019-02-21) using the SEQUEST HT algorithm as implemented in the Proteome Discoverer 2.4 software package. Data was re-calibrated using the recalibration function in PD2.4 and final search tolerance setting included a mass accuracy of 10 ppm and 50 mDa for precursor and fragment ions, respectively. A maximum of 2 missed cleavage sites was allowed using fully tryptic cleavage enzyme specificity (K, R, no P). Dynamic modifications were oxidation of Methionine, and deamidation of Asparagine and Glutamine. Dynamic modification of protein N-termini by acetylation was also allowed. Carbamidomethylation of Cysteine, TMTPro-modification of Lysine and peptide N-termini were set as static modifications.

For protein identification, validation was done at the peptide-spectrum-match (PSM) level using the following acceptance criteria; 1% FDR determined by Percolator scoring based on Q-value, rank 1 peptides only.

QUANTIFICATION AND STATISTICAL ANALYSIS

Quantification and statistical analysis LC-MS/MS

For quantification, a maximum co-isolation of 50% was allowed. Reporter ion integration was done at 20 ppm tolerance and the integration result was verified by manual inspection to ensure the tolerance setting was applicable. For individual spectra, an average reporter ion signal-to-noise of >20 was required. Further, shared peptide sequences were not used for quantification.

Protein intensities were normalized ensuring same total ion current in each quantification channel. Intensity values were then $\log_2$-transformed and aligned between treatments and replicates, so as each protein has the same mean intensity in all treatments and replicates. To estimate effect size (amplitude) and p-value (significance) of the protein hits, compound-induced protein stability changes relative to the vehicle control were evaluated using moderated t-test implemented in the limma R-package.[70] Benjamini-Hochberg correction is applied to the t-test derived p-values to adjust for multiple comparison. ns: not significant $p > 0.05$, (*) $p \leq 0.05$, (**) $p \leq 0.01$, (***) $p \leq 0.001$, (****) $p \leq 0.0001$.

Quantification and statistical analyses immunoblots

Quantification of immunoblots was performed with ImageJ 1.53c or Image Lab 6.0.1. For statistical analyses, at least three independent experiments ($n = 3$ biological replicates) were performed. p-values were calculated using one-way or two-way ANOVA in Prism version 10.3.0 (507), with $p < 0.05$ considered statistically significant. Where indicated in the figure legends, statistical significance was determined using two-way ANOVA followed by Tukey's multiple comparisons test, or one-way ANOVA followed by Dunnett's multiple comparisons test. Data are presented as the median, mean with standard deviation (SD), or mean ± standard error of the mean (SEM), as specified in the figure legends. ns: not significant $p > 0.05$, (*) $p \leq 0.05$, (**) $p \leq 0.01$, (***) $p \leq 0.001$, (****) $p \leq 0.0001$.

Statistical analyses NanoBit-Assays

NanoBit assay data were analyzed using GraphPad Prism 10.3.0 (507). Luminescence values were first background-corrected and normalized to the control condition. For comparison between two groups, an unpaired, two-tailed Student's t test was performed to determine statistical significance. All data are presented as mean ± standard error of the mean (SEM) from three independent biological replicates ($n = 3$). ns: not significant $p > 0.05$, (*) $p \leq 0.05$, (**) $p \leq 0.01$, (***) $p \leq 0.001$, (****) $p \leq 0.0001$.